An off-line tuning ion source for the optimization of the WITCH experiment

Mikael Herman Tapani Reponen

Master's Thesis

University of Jyväskylä, Department of Physics

Supervisors: Ari Jokinen, Nathal Severijns

Foreword

The experimental part of this thesis lasted altogether about four months. It was made with the WITCH experiment group at the ISOLDE laboratory in CERN during the summer 2006 and in February 2007. I would like to thank the head of the WITCH experiment Nathal Severijns for giving me the opportunity work at their experiment during my CERN summer student period and Ari Jokinen for aiding me with all the arrangements and with the thesis itself. I would also like to thank the rest of the WITCH team, Sam Coeck and Mustapha Herbane for giving me all the help I needed, and especially Valentin Kozlov for his help during the February work period. I am also grateful for the IKS K.U. Leuven for providing me an apartement during this stay.

Abstract

This work concentrates on the commissioning and characterization of a surface ion source which will be used for off-line tuning of the WITCH set-up at ISOLDE - laboratory at CERN. The ion source's properties were examined in a test set-up as well as in final set-up in the horizontal beamline of the WITCH set-up. It is found out that the only parameter affecting the beam shape is the extraction voltage and that the most symmetrical beam shape is achieved when the extraction voltage V_E is about -10.7 V. At this point the beam cross section is approximately a circle with a diameter of 8.5 mm±1 mm. This result probably contains a lot more error than 1 mm as it is also apparent that the beam is shifted from the beamline center. The V_E= -10.7 V provides beam intensities that are about one third of those provided by the best extraction voltage range V_E ∈[-5, -7] V. This kind of large drop from the maximal ion current was typical in these measurements. The measurements also reveal that the lack of power regulation in the current set-up decreases the achievable ion current up to about 80%. This affects the usability of the ion source as now only around 1000 ions could be detected at the MCP in the retardation spectrometer.

Contents

List of Tables

List of Figures

Chapter 1

Introduction

The source of new physics is nowadays usually associated with high energy particle physics such as the LHC which can test the Standard Model with un-precedent energies. However the Standard Model still has properties that can be examined precisely with low energy physics. β -decay is a very good phenomenon for tests for the Standard Model and the research field around it has already proved invaluable for the development of the electroweak theory. Major contributions of β -decay studies are for example the finding of the V-A structure with the maximal parity violation of the electroweak processes, by Valentine Telegdi in 1962 [3] and Lee and Yang [4] in 1956, and the helicity of the neutrino. The β-decay studies continue to contribute to the development of the Standard Model and currently there are numerous experiments that are trying to improve the experimental limits of the predictions made by the Standard Model. The β-neutrino angular correlation coefficient is one of the observables that yields information about the very structure of the weak interaction for example possible existence of new interaction types. This coefficient is being studied for example at the Paul trap based LPC-trap experiment [5] and at the Penning trap based WITCH experiment (**W**eak **I**nteraction **T**rap for **CH**arged particles).

To be able to improve the limits of the possible new physics, the experimental set-ups have to be very well tuned so that any error sources are reduced to minimum. In the WITCH set-up context it means that the ion transfer efficiency from the REX-TRAP to the detectors at the end of the spectrometer has to be as good as possible. In detail, this means that the tuning of each electrode has to be optimal so that the beam is transfered through each segment of the beamline with high efficiency. The tuning process also includes the optimization of dynamic electrodes such as the spectrometer and the injection in to a magnetic field. Currently the WITCH set-up is tuned using off-line ion sources from the REX-TRAP or with a small cross-beam ion source in the vertical beamline (VBL). This arrangement is not the most optimal as the cross-beam source is too weak and the REX-TRAP

ion source is not always available to testing. Thus a new off-line tuning ion source was needed.

The WITCH off-line tuning ion source's design and operation principle is almost identical to the REX-TRAP ion source. It produces ions via surface ionization from a potassium zeolite and accelerates them up to 30 keV. The surface ionization, first discovered by Langmuir and Kingdon in 1923 [6], is one of the easiest ways to produce stable ion currents with intensities up to few nA, which reduces the amount of needed space and equipment. The work done in this thesis concentrates on the properties of the WITCH off-line ion source. The main interests are the operation parameters and the shape of the ion beam produced by the ion source. The ion source is tested on a test set-up as well as in it's final set-up on the horizontal beamline of the WITCH set-up. The ion source still will require testing and tuning before it can be used with all it's potential for the WITCH set-up optimization.

Chapter 2

ISOLDE

The main laboratory for low energy nuclear physics experiments in CERN (**C**onseil **E**uropèen pour la **R**echerche **N**ucléaire) is called ISOLDE [7] which is an acronym for **I**sotope **S**eparator **O**n **L**ine **DE**vice. The facility produces about 600 radioactive isotopes of more than 60 elements [8] to be used in many different experiments within the laboratory. These experiments include nuclear physics, solid-state physics, nuclear medicine, material physics etc. The history of the ISOLDE dates back to 1967 when first experiments were made. After that it has had many upgrades, the latest being a switch from Synchro-Cyclotron (SC) accelerator to the Proton Synchrotron Booster (PSB) in 1992.

The ISOLDE facility (see Fig. 2.1), excluding the experimental hall, is considered to be high radiation area. The high radiation areas include the target area and the radioactive laboratory. These areas are well protected with concrete and metal blocks and on top of that they are buried underground. Besides the effective static protection, these areas also include a ventilation and vacuum systems which prevent radioactive gases from leaking out of the facility [8].

2.1 Proton synchrotron booster

The proton synchrotron booster is a part of the CERN accelerator architecture [10]. It receives protons from a linear accelerator and accelerates them to 1 GeV or 1.4 GeV [8] energies in 2.4 μs pulses. Each pulse consists of up to $3.2 \cdot 10^{13}$ protons and the pulses are repeated in intervals of 1.2 to 2.4 seconds. About a half of the pulses in a PS super cycle are available to the isotope production at ISOLDE with the rest going to the proton synchrotron (PS). One PS super cycle last 14.4 seconds and consists of 12 pulses which corresponds to 2.1 μA [8] direct proton current at the ISOLDE target.

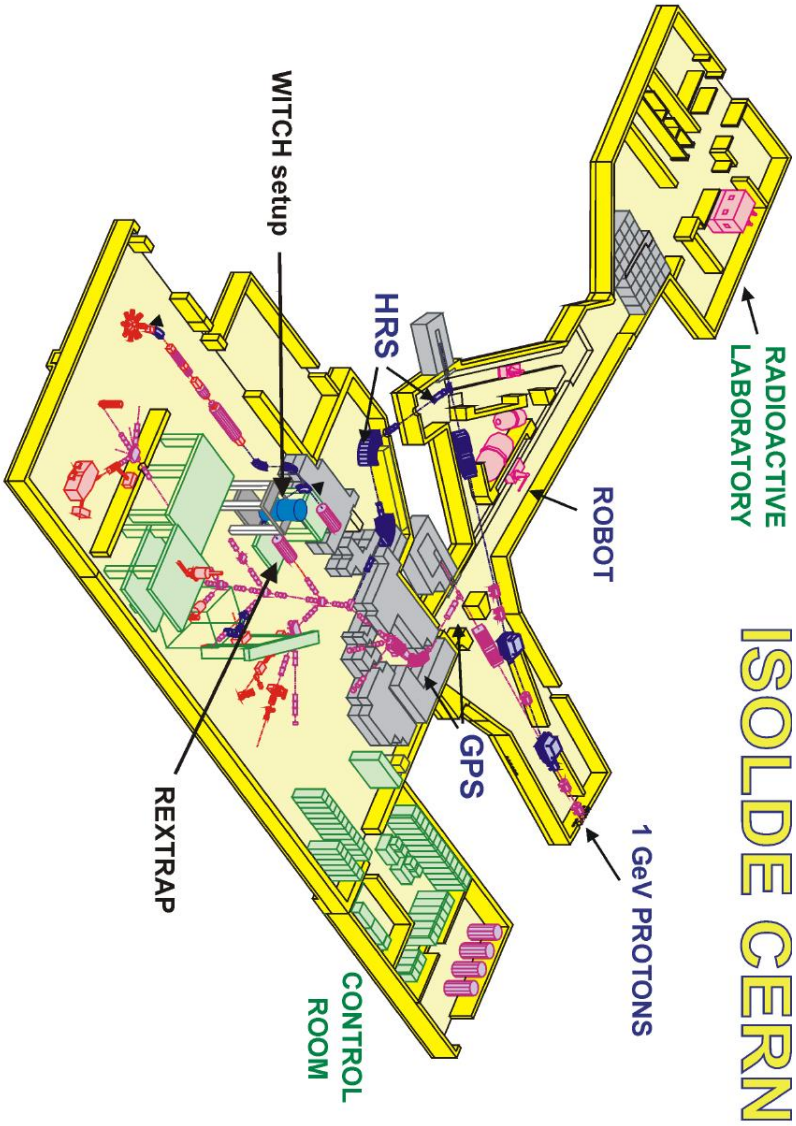

Figure 2.1: The layout of the ISOLDE facility (2000) [9]

The PSB is a significant improvement over the SC although it presents some large technological challenges. While the low repetition rate of short high intensity pulses enhances the production of radioactive isotopes, it also puts the target and target container under considerable stress due to high instantaneous power dissipation. The pulsed beam also ionizes the air around the target which in turn loads the acceleration voltage [8].

2.2 Isotope production and separation

ISOLDE uses the on-line isotope separation technique to produce pure low energy radioactive ion beams. The technique makes use of fission, spallation and fragmentation [7] to produce the radioactive isotopes at a high temperature target at the end of the PSB proton beam. The target system at ISOLDE consists of the target itself and of a ion source [8]. It produces singly charged ions from the target via surface ionization, laser ionization or plasma ionization [9]. The ions are accelerated either to 60 keV or 30 keV, and transfered in to the separators which then distribute the beam of wanted isotopes to different experiments.

The ISOLDE laboratory has two isotope separators, the General Purpose Separator (GPS) and the High Resolution Separator (HRS). The GPS is a flexible and easy to use separator with one double focusing 70° magnet. It can deliver three ion beams within 15 % from the central mass with mass resolving power of 2400. The HRS can deliver one isotope beam and it's mass resolving power can reach 6000. This resolving power is enabled by the use of two beam bending magnets in a opposite direction and elements for higher order corrections.

Chapter 3

WITCH experiment

The WITCH -experiment is a double Penning trap experiment utilizing a retardation spectrometer. It is primarily set-up to measure the recoil energy spectrum of ions resulting from nuclear β-decay [2]. This spectrum yields information about the $\beta - \nu$ angular correlation and thus [11] on the fundamental structure of the weak interaction, i.e. on the possible presence of scalar and/or tensor type charged weak currents. The main goal is to measure the angular correlation coefficient with statistical precision up to 0.5%

The elusive nature of the neutrino makes the measurement of the $\beta - \nu$ angular correlation difficult. Because of the sheer size of a neutrino detector the use of one is not possible in this type of experiment, thus the $\beta - \nu$ angular correlation has to be inferred from other observables like the recoil energy spectrum [12]. Up to now only few experiments have measured the angular correlation. The earlier experiments were based on gaseous sources [13, 14] while the later have embedded the radioactive source into a thin carbon foil [15, 16]. With these experiments the angular correlation coefficient has been measured with accuracy up to about 0.5% which is a limit that the WITCH experiment aims to reach or surpass. To achieve this precision, the WITCH experiment utilizes different techniques to avert the difficulties that accompany previous experiments. There are also other ongoing and upcoming experiments for measuring the $\beta-\nu$ correlation [17]. These include the TRIUMF experiment which uses magneto-optical traps and the Ganil experiment which utilizes a electromagnetic Paul trap.

The WITCH experiment uses a Penning trap as a radioactive source in order to eliminate the problem of recoil energy spectrum distortion associated with experiments where the β emitter is either embedded in a matter [18] or in a gaseous form. In these types of experiments the small recoil energy[1] of the daughter ions and scattering causes the ions to either completely stop in the source or at least

1. Usually less than 100 eV

it leads to distortion of their recoil energy spectrum [12]. Penning traps make the experiment more independent from the properties of the isotope of interest than experiments using other methods of trapping the ions. This is why the WITCH experiment is installed at the ISOLDE facility where a vast selection of isotopes is available [12].

The possibility of precision measurement of the recoil energy spectrum is a powerful feature as it opens up a wide range of physics for investigation [19]. The correlation coefficient yields information about the β-decay F/GT^2 mixing ratio and symmetries governing the induced weak currents [19] in addition to the β decay interaction types. The recoil energy spectrum can also be used to determine the Q -value of the decay with good precision, for example the energy dependence of a EC/β^+ -branching ratio [12] can yield new limits on the Fierz interference coefficient. The Penning trap system currently contains some β detectors that are used for normalization, but it can also be used for β and γ in-trap spectroscopy if more detectors are added [19].

3.1 Physics of the WITCH experiment

3.1.1 Standard Model

The Standard Model (SM) is a set of quantum theories that describe all known particle physics phenomenon with a common theoretical basis [17, 20]. It is a very elegant and successful model in explaining the strong, the weak and the electromagnetic interactions with a good accuracy. The theories included in the SM are the quantum chromodynamics (QCD) and the electroweak theory which includes quantum electrodynamics (QED) and the weak interaction. The gravity is the only fundamental interaction that is not included since there's yet no quantum theory of gravitation.

The Standard Model describes the behavior of the elementary particles [20] which are particles that have no known substructure. They can be divided into two groups: the matter particles and the intermediate particles of the interactions. The matter particles (see table 3.1) consist of leptons and quarks and their anti particles which both are fermions with spin of 1/2. The particles that mediate the interactions have spin 1 and they are called gauge bosons. Each interaction type has it's own type of gauge boson. Electromagnetism is mediated by a photon γ and weak force is mediated by Z and $W^{\pm}$ bosons while the strong force is mediated by 8 different gluons g_α, $\alpha = 1...8$ [20]. The main concepts that the

2. Fermi / Gamow-Teller

Table 3.1: Matter particles by generation [22]

	1st. Generation	2nd. Generation	3rd. Generation
Leptons:	Electron Electron-neutrino	Muon Muon-neutrino	Tau lepton Tau-Neutrino
Quarks:	Up Down	Charm Strange	Top Bottom

SM uses to describe the different interactions are [17] symmetries, local gauge invariances/symmetries, coupling constants and spontaneous symmetry breaking. Also the Cabibbo-Kobayashi-Maskawa (CKM) matrix [21] is worth mentioning as it describes the quark mixing phenomenon in flavor changing weak decays.

The existence of symmetries play a significant role in particle physics as they are closely linked with the dynamics a system. A physical system has a symmetry S when the system is invariant under the transformation given by S [20]. Each symmetry implies the existence of a conserved quantity [17]. For example the Noether's theorem [23] states that for every global symmetry of a Lagrangian[3] exists a current and the associated charge that is conserved [20]. The Standard Model is based on the gauge symmetry group $SU(3)_C \times SU(2)_L \times U(1)_Y$ where subgroup $SU(2)_L \times U(1)_Y$ is the symmetry group for electroweak interactions. It is the part of the Standard Model which unifies electromagnetic and weak interaction and which is the relevant symmetry group concerning the β -decay and thus the WITCH experiment. Symmetries can be classified by their symmetry transformations in the following way [20]:

1. Discrete Symmetries: The most relevant of these are the parity P, charge conjugation C and the time reversal T. These can only have discrete parameters and they are preserved separately in strong and electromagnetic interactions. The weak interaction can violate P and C separately or simultaneously [24]. There are also other symmetries that fit into this category for example the conservation of charge [17].
2. Continuous Symmetries:
   (a) Space-time symmetries
   These include the translations in space and time and rotations about an axis [17].
   (b) Internal symmetries [20]
   - Global symmetries:
   Parameters of a transformation do not depend on the space-time coordinates e.g. $SU(2)$ isospin symmetry.

3. Mathematical expression for the energy of a system

- Local gauge symmetries:
  Parameters of a transformation depend on the space-time coordinates e.g. $U(1)_{em}$ electromagnetic symmetry.

The breaking of the symmetries is as important phenomenon as the symmetries themself and one of the most important concepts is the spontaneous symmetry breaking. A definition of the spontaneous symmetry breaking states that a physical system has a symmetry that is spontaneously broken if the interaction governing the dynamics of the system has the symmetry but the ground state of the system does not [20]. One of the best known symmetry breaking mechanism is the Higgs mechanism which generates masses for the electroweak gauge bosons. Another example of the spontaneous symmetry breaking is an infinite ferromagnet. It is described by infinite set of elementary spins whose interactions are rotationally invariant but the ground state has two different situations depending on the temperature of the system [20].

In the gauge group of the electroweak interaction $SU(2)_L \times U(1)_Y$ the quark eigenstates of the weak interaction are transformed from the quark mass eigenstates of a flavor-conserving strong interaction [17, 24, 25]. This can be also thought of as a rotation of the quark states by the weak interaction. It is equivalent to the symmetry breaking mechanism that gives quarks their masses. This transformation is described by the CKM-matrix

$$\begin{bmatrix} d' \\ s' \\ b' \end{bmatrix} = \begin{bmatrix} V_{ud} & V_{us} & V_{ub} \\ V_{cd} & V_{cs} & V_{cb} \\ V_{td} & V_{ts} & V_{tb} \end{bmatrix} \begin{bmatrix} d \\ s \\ b \end{bmatrix},$$

which is expressed here as a 3×3 unitary matrix operating on the -e/3 charged d, s and b quark mass eigenstates [25]. The values of the CKM matrix elements cannot be theoretically predicted, but must be experimentally measured for example from weak decays of relevant quarks. The effect of quark mixing can be seen for example by comparing the neutron and muon decay [17].

While the Standard Model is highly successful it is hardly an ultimate theory for particle physics and it can be considered more as a low energy approximation of a more fundamental theory. It does not answer the questions for example why there is three generations of quarks and leptons or are the more than four basic forces [17]. The SM also leaves about 30 fundamental parameters without a value which includes for example the fine structure constant. The Standard Model continues to evolve with new extensions and with new constraints set to new physics [26]. While there are experiments like the WITCH which search new physics to give new directions to the Standard Model, some experiments have already found sings of phenomena that are not consistent with the Standard Model for example the

neutrino oscillation [27] and the deviations of the B_d^0- $\bar{B}_d^0$ mixing phase in B_d meson decays [28].

3.1.2 Nuclear β-decay and weak interaction

The development of the $SU(2)_L \times U(1)_Y$ electroweak part of the Standard Model is closely connected with the nuclear β-decay [29]. The nuclear β-decay studies have played a crucial role in the construction of the experimental foundations of the electroweak theory. It has been used to find and formulate the assumption of the maximal parity violation, the assumption of the massless neutrinos and the vector - axial-vector nature of the weak interaction. The nuclear β-decay continues to be important when studying the electroweak model because of it's potential sensitivity towards new physics. It also allows the possibility of choosing the quantum state of the nucleus so that the experiment can be tuned to measure a particular property of the weak interaction [30].

The β-decay takes place by β^+, β^-, electron capture and double β -decays [31]. The decay is governed by a set of selection rules for the spin and parity and in addition a separation between allowed and forbidden decays. The selection rules can be expressed as [32]

$$\begin{aligned} \Delta I &= 0, 1 \\ \Delta\pi &= \text{no} \end{aligned}$$

for allowed β decay and

$$\begin{aligned} \Delta I &= 0, 1, 2 \\ \Delta\pi &= \text{yes} \end{aligned}$$

for the first-forbidden decays. Here I is the nuclear spin and π is the parity. For the allowed decays ΔI=0 corresponds to Fermi decays and ΔI=0,1 (not $0^+ \rightarrow 0^+$) to Gamow-Teller decays [32]. This means that in the Fermi decays, the electron and neutron have antiparallel spins and in the Gamow-Teller decays they have parallel spins [31].

The nuclear β-decay process, at quark level, is mediated by the W^- -boson and as the energies involved in the interaction are typically much lower than the mass of the W -boson, the interaction can be expressed as a four fermion contact interaction [17] with a Hamiltonian

$$\mathcal{H}_{V-A} = \frac{\mathcal{G}_F}{\sqrt{2}} J_\mu^\dagger \cdot J_\mu + h.c.. \tag{3.1}$$

In this equation $\mathcal{G}_F$ is the Fermi coupling constant for the V-A theory and J_μ is a current containing both fermionic and hadronic contribution [17]. This is the Hamiltonian for the nuclear β -decay in the V-A -theory in which the maximum parity violation is present [19]. If the maximal parity violation is not assumed, the Standard Model of electroweak interaction contains many other interaction types at a fundamental level. These interaction types are in the addition to vector (V) and axial-vector (A), scalar (S), tensor(T) and pseudoscalar interaction(P) [19]. The most general from of the Hamiltonian for the β decay is [17]

$$\begin{aligned}\mathcal{H} = \; & \tfrac{\mathcal{G}_F}{\sqrt{2}} V_{ud}\Big[\left(\overline{\psi}_p \psi_n\right)\left(\overline{\psi}_e \left(C_S + C_S^{'}\gamma_5\right)\psi_\nu\right) \\ & + \left(\overline{\psi}_p \gamma_\mu \psi_n\right)\left(\overline{\psi}_e \gamma^\mu \left(C_S + C_S^{'}\gamma_5\right)\psi_\nu\right) \\ & + \tfrac{1}{2}\left(\overline{\psi}_p \sigma_{\lambda\mu} \psi_n\right)\left(\overline{\psi}_e \sigma^{\lambda\mu} \left(C_T + C_T^{'}\gamma_5\right)\psi_\nu\right) \\ & - \left(\overline{\psi}_p \gamma_\mu \gamma_5 \psi_n\right)\left(\overline{\psi}_e \gamma^\mu \gamma_5 \left(C_A + C_A^{'}\gamma_5\right)\psi_\nu\right) \\ & + \left(\overline{\psi}_p \gamma_5 \psi_n\right)\left(\overline{\psi}_e \gamma_5 \left(C_P + C_P^{'}\gamma_5\right)\psi_\nu\right)\Big] \\ & + h.c.\end{aligned} \tag{3.2}$$

The coefficients C_i and C_i' are the coupling constants for the interaction types i=(S, V, T, A, P). The γ_i's are Dirac's gammafunctions and

$$\sigma_{\lambda\mu} = -\frac{i}{2}(\gamma_\lambda \gamma\mu - \gamma\mu\gamma_\lambda) \tag{3.3}$$

is a tensor operator. V_{ud} is the ud'th.-matrix element of the CMK matrix (see sec. 3.1.1)[29].

The coefficients C_i and C_i are among those parameters in the SM that have to be deducted from measurements. So far only the vector and axial vector interactions have been observed, but the scalar and tensor interactions have not been ruled out with high precision [12]. The values of these coefficients are mostly determined by measuring the β-neutrino angular correlation for the β- decay which can be approximated to be [19]

$$\omega(\theta_{\nu\beta}) \approx 1 + a\frac{v}{c}\cos\theta\left(1 - \frac{\Gamma m_e}{E}b\right), \tag{3.4}$$

for an unpolarized nuclei. Here E is the total energy of the β-particle, $\theta_{\nu\beta}$ is the angle between the β-particle and the neutrino, m_e is the mass of the electron, v/c is the velocity of the β particle and $\Gamma = \sqrt{1-(\alpha Z)^2}$. The α is the fine structure constant and Z the nuclear charge of the daughter nucleus. The Fierz interference coefficient b is approximated to be zero based on experiments [12]. The variable a in the equation 3.4 is the angular correlation coefficient which, for pure Fermi decays, can be expressed approximately as

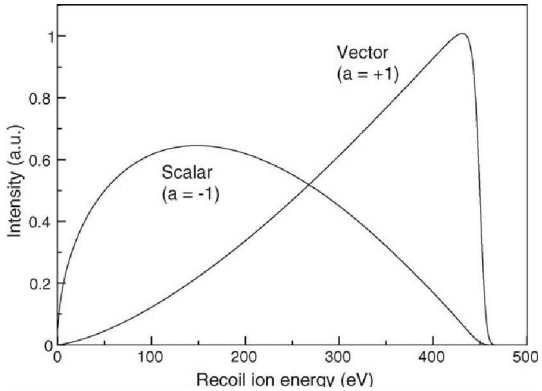

Figure 3.1: Calculated differential recoil energy spectrum for V and S interactions [18]

$$a_F = 1 - \frac{|C_S|^2 + |C'_S|^2}{|C_V|^2} \tag{3.5}$$

and for pure Gamow-Teller decay as

$$a_{GT} = -\frac{1}{3}\left(1 - \frac{|C_T|^2 + |C'_T|^2}{|C_A|^2}\right). \tag{3.6}$$

It can be shown [12] that the vector interaction V can only take place between particle and antiparticle with opposite helicities and scalar interaction takes place when the helicities are the same. Therefore in the superallowed Fermi decays ($0^+ \rightarrow 0^+$) in which the β and neutrino spin couple to zero the antiparticle and the particle are emitted into same direction for the vector interaction whereas the scalar interaction would cause the particles to be emitted into opposite directions [19]. This on average leads for relatively larger recoil energy for the vector interaction than for the scalar interaction (see Fig. 3.1). According to the Standard Model only vector interaction can contribute to the decay rate which means that the value of the angular correlation coefficient becomes 1 in the case of pure vector interaction. Any admixture of scalar and vector interaction would lead to values of $a<1$, thus by measuring the angular correlation coefficient a one can deduct which interactions contribute in the β-decay [12].

3.2 Set-Up

3.2.1 REX-TRAP

The first relevant part of the WITCH set-up is the REX-TRAP (see Fig. 3.2) [33]. It is actually a part of a bigger experiment called the REX-ISOLDE [34] which is a pilot experiment for post acceleration of radiactive ions. The REX-TRAP is a Penning trap that is used to accumulate, bunch and cool the ions from the ISOLDE beam or from the REX-TRAP off-line ion source. It also improves the emittance of the beam from $35 \cdot \pi \cdot \text{mm} \cdot \text{mrad}$ of the original ISOLDE beam to $10 \cdot \pi \cdot \text{mm} \cdot \text{mrad}$ [9]. The trap has two parts, a cooling part with high buffer gas pressure and a trapping part with a potential minimum. Before the ions enter the Penning trap they are decelerated electrostaticly from 60 keV to only few eV by using a high voltage platform. The decelerated ions pass the potential barrier of the Penning trap which is located inside a 3 Tesla superconducting solenoid. The first part of the trap is filled with Ar buffer gas at 10^{-3} mbar which slows the ions down by collisions between the ions and the atoms in the buffer gas. After the ions are reflected from the potential barrier at the end of the trap they begin to oscillate between the trap end caps and eventually accumulate in the potential minimum. Finally they are subjected to RF-sideband cooling [9] . The REX-TRAP ejects the ion bunches at 30 keV with about 50 Hz repetition rate when it's used for REX-ISOLDE and about 1 Hz repetition rate when used for the WITCH experiment [9]. The trap also includes a surface ionizing ion source that is used for off-line tuning of the REX-ISOLDE and for the WITCH experiment.

3.2.2 Beamlines

The WITCH beamlines are the first part of the set-up that are solely used by the WITCH experiment. Their purpose is to transfer the ions from the REX-TRAP and prepare them for the injection in to the spectrometer and in to the surrounding magnetic field [9]. The beamlines are made of a stainless steel tube with 60 mm internal diameter. They mostly contain electrodes, Einzel lenses and diagnostics equipment which are used to steer, focus and monitor the ion beam so that the transfer trough the beamlines could be made to be as efficient as possible. The vertical beamline also houses retardation and drift electrodes that are used to reduce the ion energy before they enter the spectrometer [2]. Both beamlines have a vacuum system which provides a vacuum of about 10^{-7} mbar or better.

The beamline is composed of two different parts called the horizontal and the vertical beamline which will be called from now on the HBL and the VBL, respectively. The HBL (see Fig. 3.3) begins after the REX-TRAP and it's main

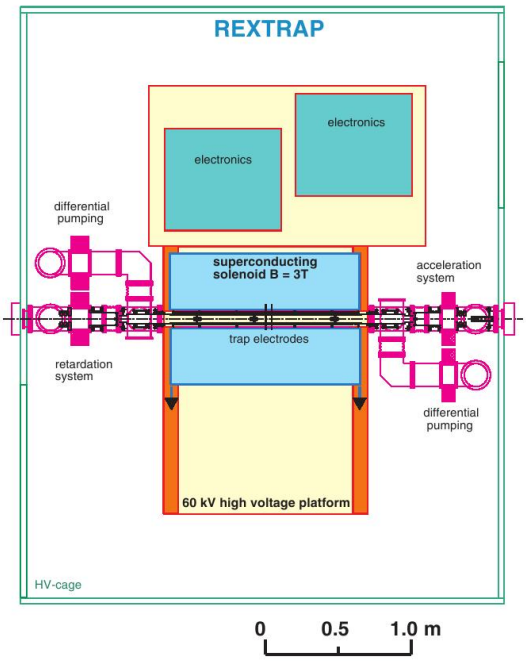

Figure 3.2: The REX-TRAP [35]

elements are two kicker-bender combinations and the WITCH off-line ion source. The elements are used to turn the beam first 29° and later 90° [2]. The kickers consists of two parallel 60 mm^2 plates with 3 cm gap that are both at 3.75° angle in respect to the beam. Their purpose is to either guide the beam into the bender when at suitable potential or let it pass trough. The benders are made of two spherical electrodes with radius of 385 mm and 415 mm. They ensure that when a beam is bend at radius of 400 mm it is also focused in the perpendicular to the deflection plane [2]. In addition, the kicker-bender elements contains a pair of steerer electrodes to correct the beam direction [9]. Between the two kicker-bender elements is an Einzel lens which focuses the ion beam with an electric field. A simple Einzel lens consists of three or more cylindrical or rectangular prisms in series [36]. The WITCH set-up Einzel lens can be seen in figure C.3(a). All of the electrodes and Einzellenses in the HBL work on static voltages [9] which are only changed for tuning purposes.

The VBL (Fig. 3.4) begins after the 90° bender and it contains electrodes that are used to retard the ion bunch energy down from 60 keV to 1.5 keV. The retardation has to be done in order for the Penning trap to be able to trap the ions. This requires that the ion energy is scaled even further down from 1.5 keV to about 50 eV [2]. The retardation could be done by putting the traps and the spectrometer

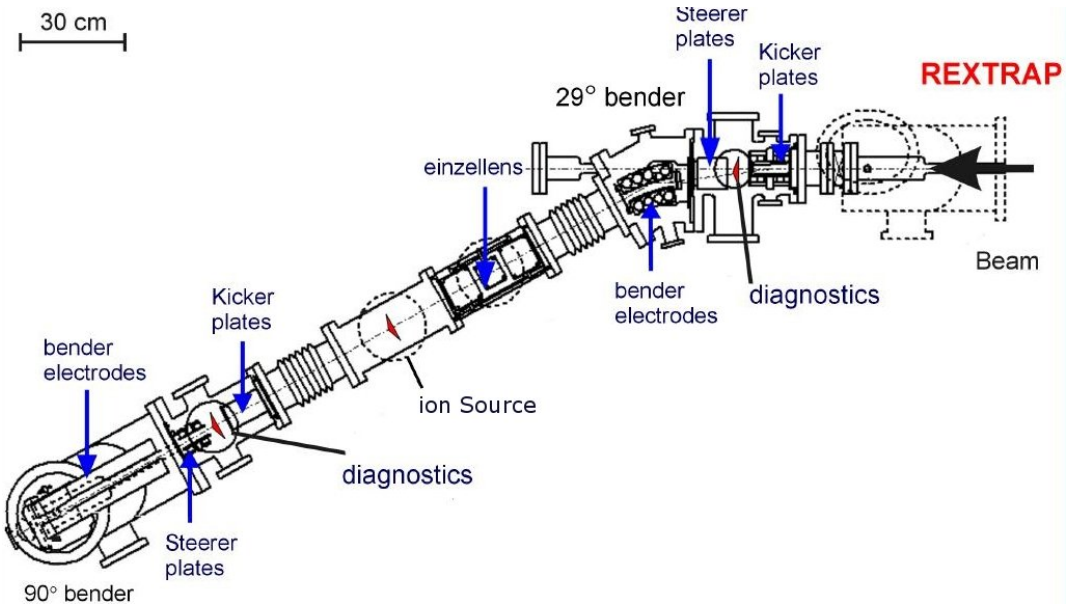

Figure 3.3: The horizontal beamline of the WITCH set-up [9]

to 60 kV high voltage platform or with a pulsed drift cavity and retardation electrodes. Only the latter is a practical approach in the WITCH experiment due to the construction of the experiment. The pulsed drift section in the WITCH experiment is called the PDT which is based on a pulsed drift cavity used in the ISOLTRAP [37] experiment. The PDT works by changing the potential energy down without changing the kinetic energy while the ions are inside the tube. This changes the total energy of the ion, and in WITCH experiment it is done so that the total energy is zero after the PDT [9]. The potential energy is switched down from 52 kV to -8 kV when the 60 keV beam energy is used at WITCH. After the PDT the VBL has multiple steering and drift electrodes and an Einzel lens to guide the beam into the magnetic field so that they are perpendicular to each other. If the beam has a component that is not perpendicular to the magnetic field, some of the ions enter to an unfavorable trajectories inside the Penning traps or are reflected completely away from the traps.

Diagnostics equipment

Both of the beamlines have diagnostics units that are used to monitor the beam [2] and to help with the tuning process. The diagnostics units consist of MCP detectors, collimators and Faraday cups which provide numerous means to monitor the beam position and shape

The collimators are for example metal strips which have round and/or rectangular

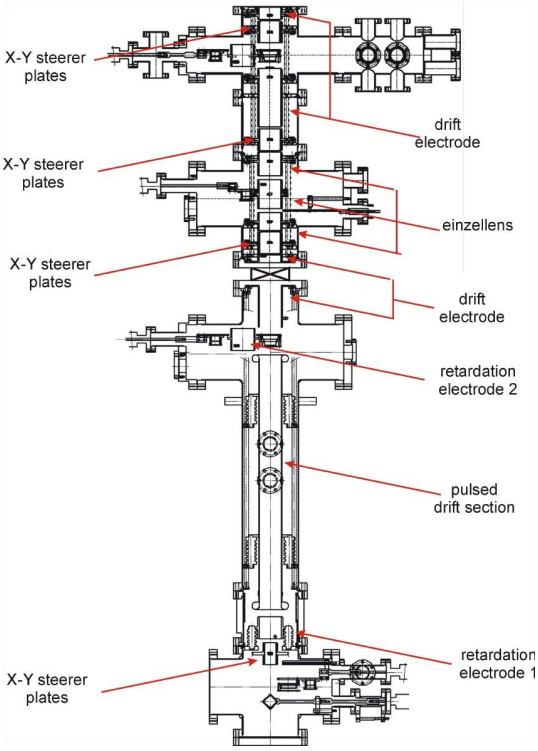

Figure 3.4: The vertical beamline of the WITCH set-up [2]

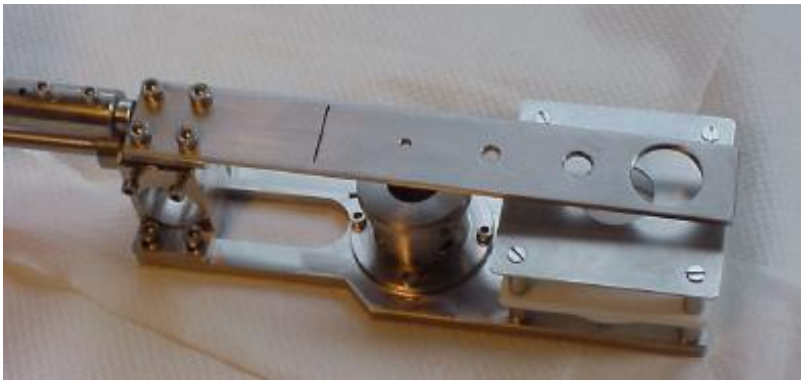

Figure 3.5: The collimator strip system [2]

holes of different sizes. They are used in conjunction with the MCP and Faraday cups by blocking the part of the beam with the collimator and measuring the corresponding ion current on the detector. The WITCH HBL diagnostics unit has a collimator strip with circular holes with 20 mm, 8 mm, 5 mm and 3 mm diameter and a 20×1 mm^2 slit (see Fig. 3.5). The collimator strip is mounted on the HBL diagnostics unit in front of the Faraday cup and the MCP.

The detector system of the diagnostics units consists of MCP's and Faraday cup's which both only work as a ion counter without energy sensitivity. The Faraday cup is a simple stainless steel cup with an anode and a repeller electrode [2] or in some cases a magnetic field [38]. As a positive ion hits the Faraday cup, it removes an electron from the cup which causes a measurable current. The ion impact also causes secondary electrons to be emitted from the cup which must be reflected back to the cup with either a repeller voltage or a magnetic field. A repeller voltage of few ten's of volts is sufficient to repel the secondary electrons back to the anode [2]. Without any repelling the measured ion current would be about two times larger than the real current. The HBL diagnostics unit includes also a split anode Faraday cup. The anode has been split into 9 vertical segments which allow beam intensity measurements in horizontal direction even though the cup can only be moved in vertical direction. The diameter of the Faraday cups in the WITCH set-up and the WITCH ion source test set-up is 16.5 mm.

The Faraday cups are used to measure continuous ion currents of the order of 1 pA but a choice for low intensity, pulsed ion currents is the MCP detector. It consists of a glass plate that has many small parallel holes typically at about 10° angle with the surface, coated with semiconducting material (see Fig. 3.6) [2]. This construct turns the channels into electron multipliers and by using multiple plates the sensitivity of the detector can be increased. Typically the channels are 10-100 μm wide with from 40 to 100 length to diameter ratios [39]. The secondary

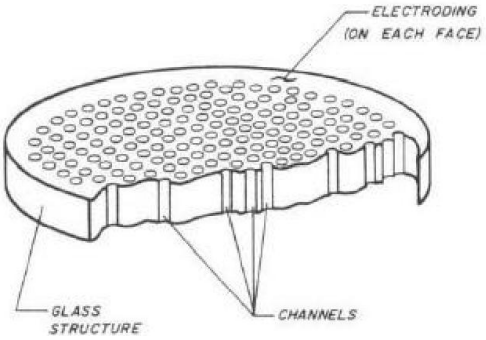

Figure 3.6: A cutaway picture of a MCP detector[39]

electrons created in these micro-multipliers are accelerated by about 1 kV potential difference between the front and the back of the plate and collected with an anode behind the plate. In the case of the WITCH experiment the diameter of the MCP is 20 mm and the anode is segmented into 10 by 10 wire grid where each wire is 1 mm wide and spacing between the wire is 1 mm [40]. Only nine of these wires are used for measurements. The grid is made of two perpendicular sets of wires marked A and B with the A set being parallel to the HBL and the wire numbering running from left to right from the beam direction (see Fig. 3.3). The B wire numbering runs towards the REX-TRAP. While the grid reduces the measured intensity by about an order it gives the MCP position sensitivity.

Diagnostics units for the HBL and the VBL are presented in figure 3.7. In both units the Faraday cup and the MCP are mounted on a same support. In the HBL diagnostics unit the support is on a linear feedthrough, which position can be controlled with high precision, and in the VBL unit the support is on a less precise sliding support. The collimator strip on the HBL unit is mounted on a separate linear feedthrough. All the linear translators are made by Caburn-MDC [2]. The HBL diagnostics unit is placed after the WITCH ion source and the VBL unit is right after the 90° bender.

3.2.3 The WITCH Penning traps

Electromagnetic particle traps are widely used in precision mass measurements and in radiation spectrometry as well as in precision measurements of the natural constants [41]. The purpose of ion traps is to focus and center the ions to as small a volume as possible with as small momentum as possible. This means the minimization of the six-dimensional phase-space $(\vec{r}, \vec{p})$ where $\vec{r}$ is the position vector and $\vec{p}$ is the momentum vector. The ion momentum is decreased by cooling the ions via different methods which reduces the 1 st. and 2 nd. order Doppler

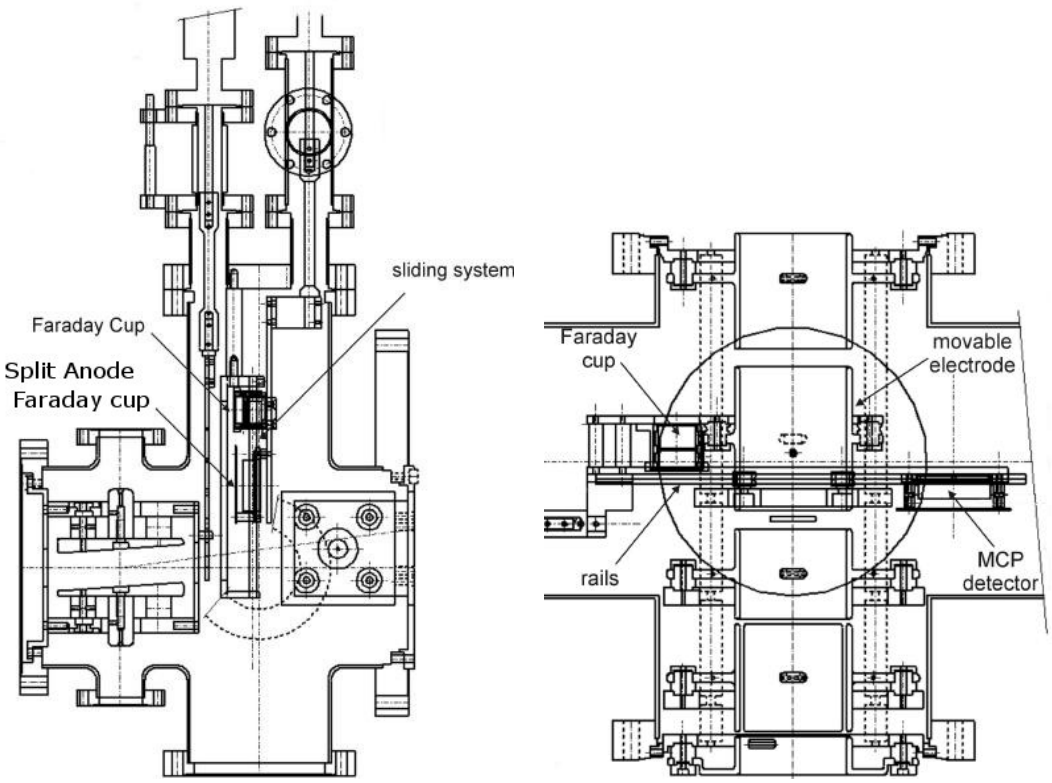

(a) (b)

Figure 3.7: The WITCH HBL (a) and the VBL (b) diagnostics units

effects and centers the ions to the middle of the trap. In addition to cooling, the centering of the ions to a wanted volume requires focusing which is done by applying a external electromagnetic force to the ions. Size and position of the trapped ion bunch is known with very high accuracy. The only forces acting on the trapped particles are those forces which return the ions to a wanted volume, when they approach the border of that volume because of the momentum they have left.

The main different types of trapping methods are the Paul trap and the Penning trap. The other trapping methods utilize the magnetc and/or optical properties of a atom or a ion[4]. The latter utilizes, for example, a laser to cool the ions and traps them by taking advantage of their electrical or magnetic dipole moments and using electromagnetic multi-pole fields and Zeeman and Stark effects. The use of these techniques allow the trapping of neutral atoms for example in a optical trap called a ZOT[5] trap [41]. These kind of neutral particle traps are also called magnetic bottles.

The Paul trap is a close relative to the Penning trap. It's a three-dimensional quadrupole trap that uses such a geometry which produces hyperbolical trap by using an electric field with a static and a dynamic component (Radio Frequency (RF)). A magnetic field can be added to produce a so called combined trap which is not a pure Paul trap [41]. A Paul trap is an ideal trap for applications which only require ion storage or precision radiation spectroscopy and it's lack of a magnetic field makes it a fine choice for metrology[6]. An electrode structure for a simple Paul trap is presented in figure 3.8(a). The shape of the both electrodes is hyperbolical which means that their shape is defined by equations [1] $z^2 = \frac{1}{2}(\rho^2 - \rho_0^2)$ for the ring electrode and $z^2 = \frac{1}{2}(\rho^2 + \rho_0^2)$ for the end electrodes. When the ring shape fulfills the condition $\rho_0^2 = 2z_0^2$, the geometry produces an electric potential[41] of form

$$\Phi = \frac{\Phi_0}{2}\frac{\rho^2 - 2z^2}{\rho_o^2}, \tag{3.7}$$

where $\Phi_0/2 = V_{dc} - V_{ac}\cos(\Omega t)$ is the potential on the ring electrode, Ω is the angular frequency of the static and RF-component, the potential of the end electrodes is $-\Phi_0/2$ and ρ and z are the radial and axial parameters of a hyperbolical surface on a $\rho - z$ -plane. $2\rho_0$ and $2z_0$ denote the inner ring diameter and the closest distance between the end electrodes [42] from which it follows $\rho^2 = x^2 + y^2$. This configuration causes the ions to move in a way which can be de-constructed

4. Magnetic, Optical or Magneto-optical traps
5. Zeeman-Shift Spontaneus-Force Optical Trap
6. The science of measurement

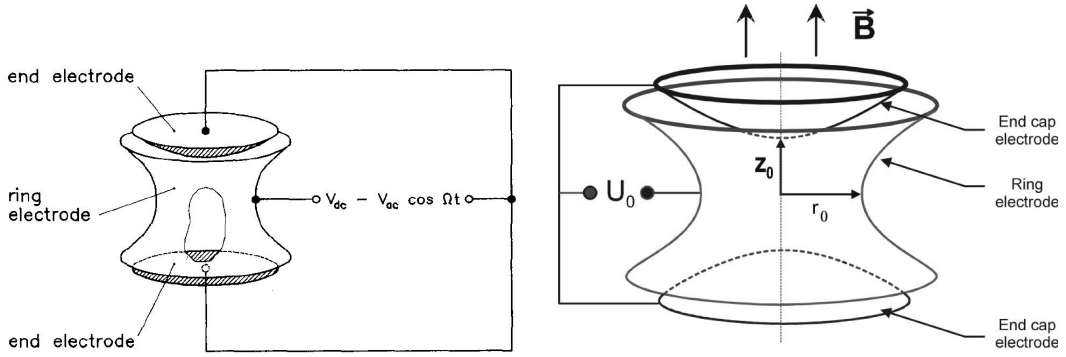

(a) (b)

Figure 3.8: Electrode structure of a Paul trap [1] (a) and of a Penning trap [2] (b)

into three components [43]: micro-motion oscillation and radial axial components of a secular oscillation. The frequency of the micro-motion is the same as the electric field Ω (also know as the driving frequency) and the frequency of the secular oscillation is typically about a tenth of that. The frequency of the latter is almost independent of the ion mass and the oscillation takes place in a pseudopotential well created by the oscillating electric field.

If the electric potential in the electrodes in the Paul trap is connected in such a way that it only includes a DC-voltage $\pm U_{dc}$, and with such a polarity that the particles begin to oscillate in the z- direction with a frequency

$$\omega_z = \sqrt{\frac{4QU}{m\rho_0^2}}, \tag{3.8}$$

the particles become unstable in $x-y$ -direction [41]. To overcome this instability a magnetic field $\vec{B}$ must be applied. The field causes the ions, with $\frac{q}{m}$ charge to mass ratio, to perform a circular motion with an angular frequency

$$\omega_c = \frac{q}{m}B \tag{3.9}$$

due to Lorentz force [42]. The symbols used here have the same meaning as in the Paul trap examination. The ions are confined in a electric potential of

$$\Phi = \frac{U_{dc}}{2d^2}\frac{z^2 - \frac{\rho^2}{2}}{\rho_o^2} \tag{3.10}$$

in axial direction and in x-y direction by a magnetic field. The $d^2 = \frac{1}{2}\left(z_0 + \rho_0^2/2\right)$

is a measure for the characteristic trap dimensions [42]. The electrode structure of a simple Penning trap is displayed in figure 3.8(b).

By solving the equations of motion

$$m\ddot{z} = qE_z \tag{3.11}$$

and

$$m\ddot{\vec{\rho}} = q(\vec{E}_\rho - \dot{\vec{\rho}} \times \vec{B}) \tag{3.12}$$

for the particle in a electric field, with components

$$E_z = \frac{-U_{dc}}{d^2} z \tag{3.13}$$

and

$$\vec{E}_\rho = \frac{U_{dc}}{2d^2} \vec{\rho}, \tag{3.14}$$

three uncoupled motion modes emerge that describe the ion motion in an ideal Penning trap [42]. The eigenfrequency's of the different solutions are [2]

$$\omega_z = \sqrt{\frac{eU_{dc}}{md^2}} \tag{3.15}$$

and

$$\omega_\pm = \frac{1}{2}\left(\omega_c \pm \sqrt{\omega_c^2 - 2\omega_z^2}\right), \tag{3.16}$$

where $\omega_c = \frac{QB}{m} f$ is the ideal cyclotron frequency [41]. These frequencies are solely determined by the trap parameters with the conditions for a stable confinement of $\frac{|q|B^2}{m^2} > \frac{2|U_{dc}|}{d^2}$ and $qU_{dc} > 0$. The different modes of motion are: [42]

1. The Harmonic trapping motion along the trap axis with the axial oscillation frequency ω_c.
2. The reduced cyclotron motion and magnetron motion frequencies ω_+ and ω_-. These frequencies are the result of the modifications made to the radial motion of a charged particle in a homogenous electric field. The modifications are caused by the radial outward pointing electrostatic field from the trapping potential.

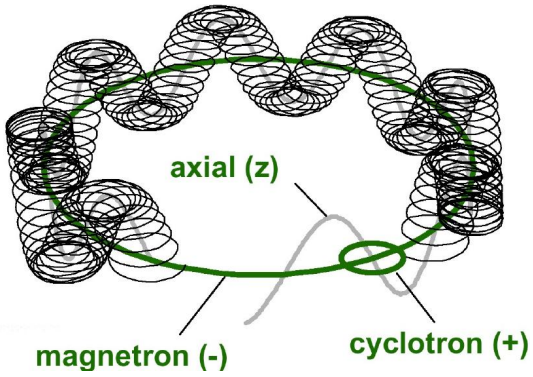

Figure 3.9: Ion motion modes in a Penning trap [2]. The magnitudes of the frequencies follow the order $\omega_- < \omega_z < \omega_+$.

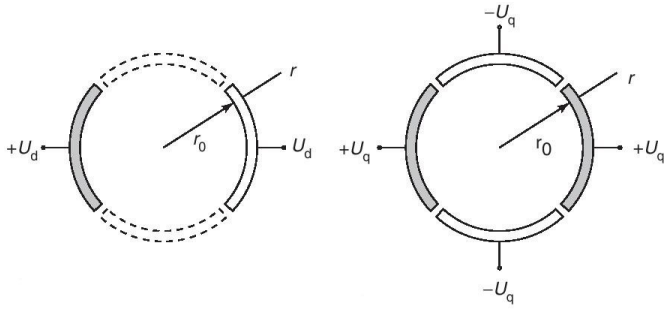

Figure 3.10: Ring electrode segments for the dipole exitation (left) and for the quadrupole exitation (right) in a radial plane [42]

The motion modes are illustrated in figure 3.9.

While the motion of the particles in the Penning trap makes them less easily centerable than particles in the Paul trap, the frequencies that they oscillate with provide a very good tool for mass spectrometry. This is because the magnetron motion frequency does not depend on the mass of the trapped particle in the first order approximation. Thus by applying proper excitations the ion motions can be altered so that different masses are separated. These excitations are realized by applying time dependent RF frequencies to the ions for example by splitting the ring electrode into 2 segments. In this way one can alter the motion of all or just some motion modes [2] by adjusting the RF frequency to that of the motion. The most common types of excitations are dipole and quadrupole excitations which can be achieved with electrode segmentations displayed in figure 3.10.

Dipole exitation is used to excite one of the ion motions in a radial plane by

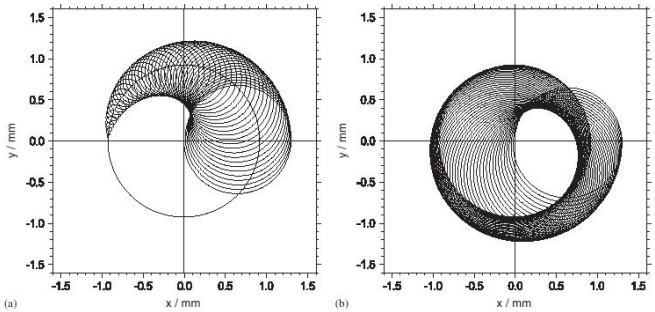

Figure 3.11: Conversion of a pure magnetron motion (solid circle) into a pure cyclotron motion in the case of azimuthal quadrupole excitation. Part (a) shows the first and part (b) shows the second half of the conversion [42]

applying a dipole electric field

$$\vec{E}_x = \frac{U_d}{a} cos(\omega_d t - \phi_d)\vec{e}_x \tag{3.17}$$

with a frequency ω_d. Although the initial change to the ion motion depends on the relative phase difference between the ion motion and the RF-field, the dipole excitation always causes the ion motion radius to increase on the longer time scale [2]. This property of the dipole excitation allows the mass selective manipulation of a ions by selecting the frequencies as $\omega_d = \omega_+$ because the reduced cyclotron frequency ω_+ is mass dependant. On the other hand all the ions can be manipulated at once by selecting the frequency ω_d to be the same as the magnetron frequency ω_- which is mass independent to first order.

Quadrupole excitation is used to couple the magnetron and the reduced cyclotron motion by using a RF modulated electric field of form [42]

$$\vec{E}_x = \frac{U_q}{2a^2} cos(\omega_{RF} t - \phi_{RF}) y\vec{e}_x \tag{3.18}$$

$$\vec{E}_y = \frac{U_q}{2a^2} cos(\omega_{RF} t - \phi_{RF}) x\vec{e}_y, \tag{3.19}$$

where $\omega_{RF} = \omega_+ + \omega_- = \omega_c$ and U_q corresponds to the maximal RF potential on a circle with radius a. In this case the magnetron motion is converted into the reduced cyclotron motion and back (see Fig. 3.11) with a time period of [2]

$$T_b = \frac{3\pi a^2}{U_q} \frac{q}{m} (\omega_+ - \omega_-). \tag{3.20}$$

Cooling is a one important part of the particle manipulation in a Penning trap and can be done in multiple ways. These methods include resistive cooling and stochastic cooling which use a external electric circuit to cool the particles down via image charges. These and other methods like laser cooling, radiation cooling etc. are explained more thoroughly in [42]. The ions in the WITCH Penning traps, like in the REX-TRAP, are cooled by using a method called the buffer gas cooling [41]. The cooling of the cyclotron motion, via the ion collisions with the buffer gas atoms, cools the magnetron motion because they are coupled. This kind of cooling works best for such motion modes like magnetron motion which is loosely coupled to it's surroundings and it has a slow and large amplitude. Cooling of the magnetron motion requires the use of the quadrupole excitation due to increase of the radius of the magnetron motion which would eventually lead to the ion escaping from the trap. The effect of the buffer gas cooling on the ion motion radius with and without a quadrupole field applied is illustrated in figure 3.12. In the buffer gas cooling ions lose energy in collisions with the buffer gas atoms, which in the WITCH case are helium atoms which minimizes energy losses due to charge exchange. The effect of these collisions to the ion motion can be described as a viscous drag force [42]

$$\vec{F} = -\delta m\vec{c}, \tag{3.21}$$

where $m\vec{v}$ is the ion momentum and $\delta(m, q, P, T, K_{ion})$ is a damping parameter which depends on the ion's charge q, mass m and ion mobility K_{ion} , and on the pressure P and temperature T of the buffer gas. The viscous drag force causes a damping of type

$$\rho(t) = \rho_0 e^{-\alpha t}, \tag{3.22}$$

where $\pm\alpha = \pm\delta\frac{\omega_\pm}{\omega_+ - \omega_-}$ is the damping constant in the case of magnetron and cyclotron motion.

The WITCH Penning traps (see fig.3.13(a)) are located after a retardation section to cool, trap, and store the radioactive ions during the measurement. The traps are in a 9 T magnetic field which requires precise injection into the magnetic field and into the traps in order to avoid deflection. The ion injection into the first Penning trap is done by lowering the bottom end-cap voltage so that the ions can pass over the potential barrier after which the potential is raised to the original value. The Penning trap electrode structure is presented in figure 3.8(b). The ions stay in the trap until they have been sufficiently cooled and centered after which they are transfered to the decay trap. This is done by lowering the upper end-cap voltage in the cooler trap and lower end-cap of the decay trap so that the ions can move to the decay trap via the differential pumping barrier. The purpose of this barrier is to prevent the buffer gas from leaking from the cooler trap into the decay trap in excess amounts. Finally the Penning trap electrodes are lowered in

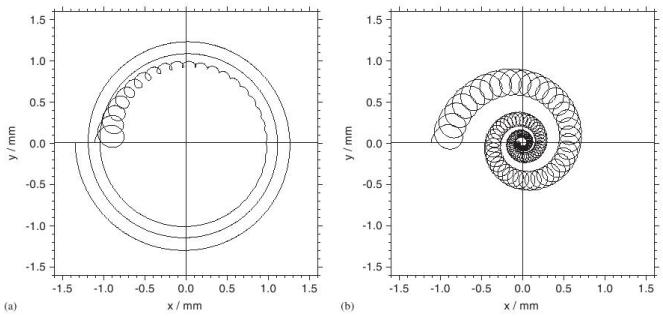

Figure 3.12: Ion trajectories in a plane perpendicular to the magnetic field in a buffer gas. (a) No excitations are applied and while the cyclotron motion is damped, the magnetron radius increases. (b) When quadrupole excitation is applied both magnetron and cyclotron motion are damped, and ions are centered [42]

such way that the ions that are still in the decay trap are injected backwards in the vertical beamline.

3.2.4 WITCH retardation spectrometer

Final part of the the WITCH experiment is a retardation spectrometer (see Fig. 3.14) that measures the energy spectrum on the recoil ions. This kind of special spectrometer is needed because the recoil ions have very low kinetic energy, usually only about few hundred eV's [9] and in addition to this, the energy is distributed between radial and axial motion.

The retardation principle is as follows. The spectrometer applies an electric potential on the ions so that only the ions with a energy higher than that can reach the detector. By changing the voltage a different number of ions reach the detector and thus one can scan the whole integral recoil energy spectrum [9]. The detector that is used at the retardation spectrometer is a MCP-MA25 detector made by Delmar Ventures [45]. This detector is not energy sensitive so it only counts the number of the arriving ions.

Because the recoil ions leaving the decay trap have both axial and radial kinetic energy, the radial kinetic energy must be converted into axial energy because the retardation only works on axial energy [9]. To make this conversion, the Penning traps and the spectrometer are placed in a magnetic field in such a way that the traps are located in a 9 T magnetic field and the spectrometer in a 0.1 T magnetic field. This kind of setup allows the use of the adiabatic invariance of the magnetic

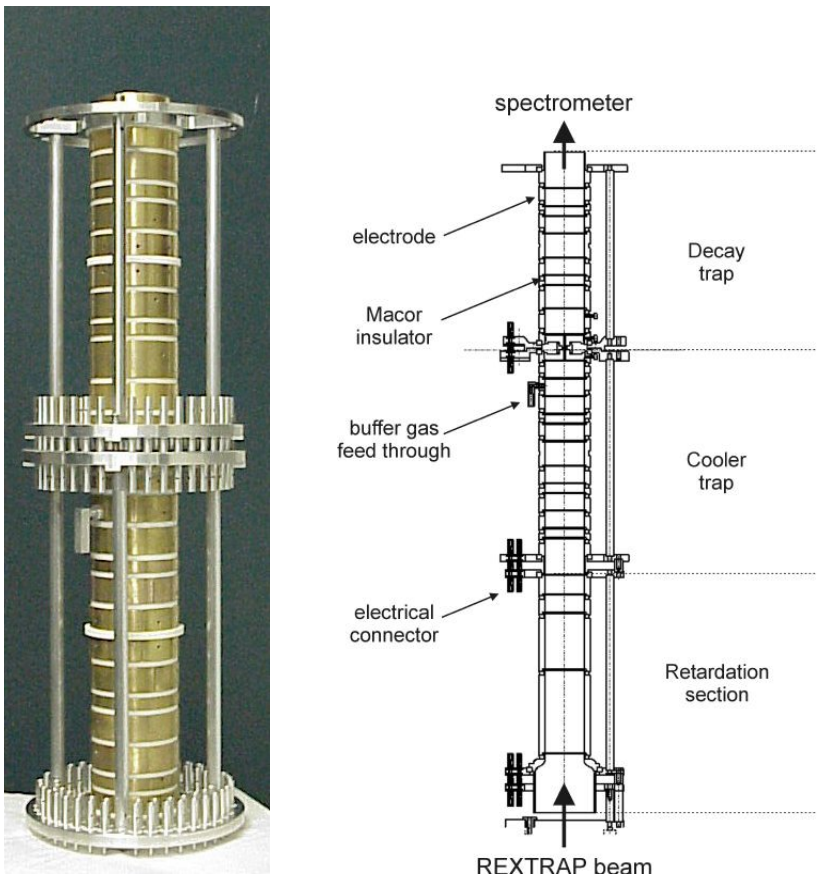

(a) (b)

Figure 3.13: (a) The WITCH Penning traps [44]. The lower part is the cooler trap and the upper is the decay trap. (b) The WITCH Penning trap electrode structure [2] for the cooler trap, the decay trap and the retardation section.

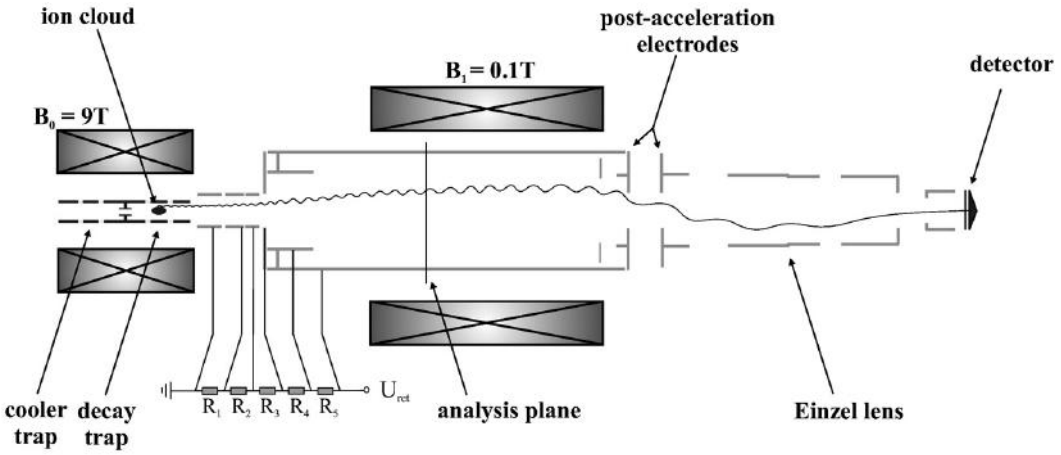

Figure 3.14: The WITCH retardation spectrometer [44]

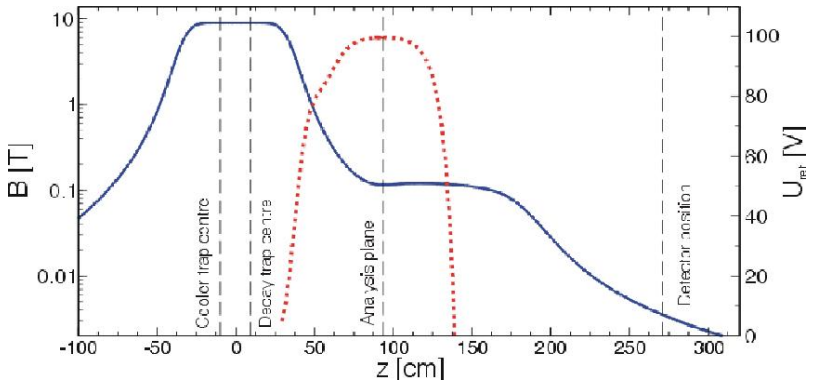

Figure 3.15: The calculated magnetic field (solid line) and retardation potential(dashed line) profile [9]

flux which in this case means that ratio of the magnetic fields

$$1 - B_{min}/B_{max} \approx 90 \tag{3.23}$$

defines the percentage of the radial energy that is converted into axial energy [9]. The magnetic field change must be small during one cyclotron turn for the energy conversion to be adiabatic.

The retarding electric field is applied so that it is parallel to the magnetic field in the space occupied by the recoil ions. It is also preferable that the retardation potential is applied as soon as the recoil ions leave the high magnetic field region while care should be taken to apply it slow enough that the ions are not reflected back due to incomplete energy conversion. The field profiles and relative positions are illustrated in figure 3.15. This ensures that the energy conversion is adiabatic

and that the ions can pass the analysis plane. Analysis plane is the name for the region where the ions experience full energy conversion and where the retardation potential reaches it's maximum. After this plane the ions are accelerated to about 10 keV energy so that they leave the magnetic field lines and are focused to the MCP by an Einzel lens. The extra acceleration and the focusing ensures a constant detection efficiency for all recoil energies and prevents the majority of β-particles from reaching the detector. On the other hand this also increases the ion beam radius which in turn means that the MCP must also be large [9].

3.3 Measurement cycle

The WITCH experiment works by continously repeating the same measurement cycle each time for a different ion bunch. The overview of one cycle is presented in figure 3.16. The measurement cycle begins in the REX-TRAP with accumulation of the radioactive ions for a time t_{acc} after which the ions are cooled with the buffer gas in combination with a quadrupole RF excitation for a time t_{coolR} [2]. The ions are ejected from the REX-TRAP with 30 keV energy in a bunched mode in to the HBL of the WITCH set-up from where they are transfered to the VBL. Before the ions enter the first of two Penning traps their energy is retarded from 60 keV to 50 eV by the PDT and by the retardation electrodes.

After retardation the ions are injected to the first of the two WITCH Penning traps called the cooler trap for a time of t_{cool}. From here the ions are transfered into the decay trap for a time t_{meas}, typically 1.5 s, so that a significant part of them has decayed. The resulting recoil ions, which typically have energy up to few hundred eV, and which are emitted in the good direction are able to leave the trap and enter to the retardation spectrometer and can finally be detected at the MCP. After the measurement period t_{meas} the ions still in the decay trap are ejected backwards to the VBL.

The measurement cycle period t_{meas} is defined by the maximum of t_{prep} (see Fig. 3.16) and t_{meas} [2] because the preparation of a new ion bunch can begin while the previous ion bunch is still in the decay trap. The overall measurement time depends of the properties of the ion, the effeciency of the set-up, the number of ions in a single bunch and of the requirement that the experiment should yield information with statistical precision of the order of 0.5%. The simulations have shown that bunches containing 10^6 ^{35}Ar ions require measurement time of 3.6 days [19] when the total transfer efficiency of the set-up is 0.5%.

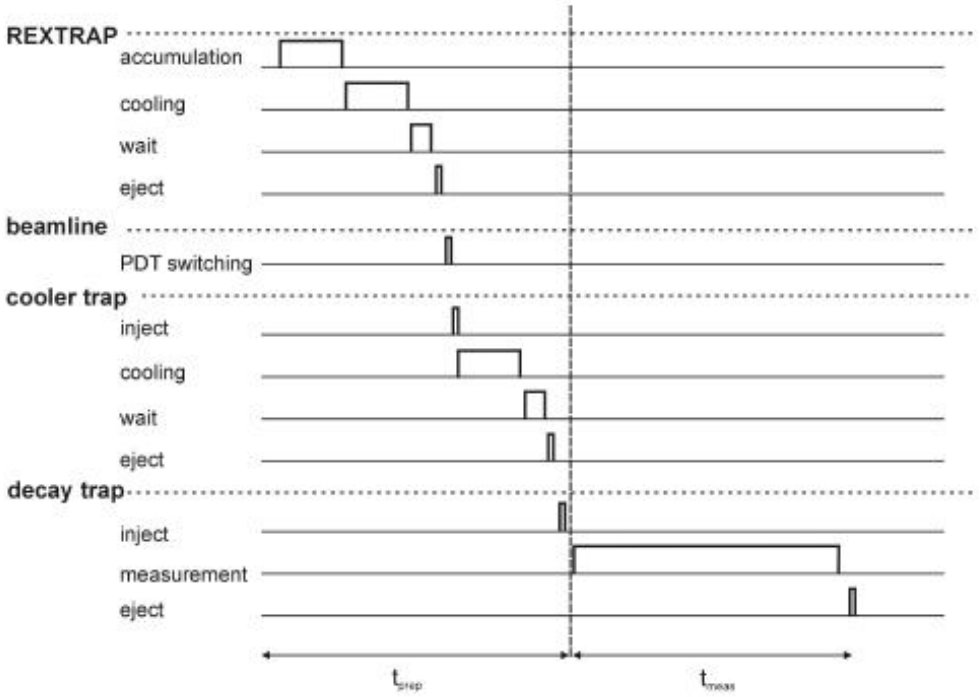

Figure 3.16: Different stages of the WITCH experiment measurement cycle. Time axis not to scale [2]

Chapter 4

Theory

4.1 Positive surface ionization

Surface ionization as a phenomenon was discovered by Langmuir and Kingdon in 1923 when they noticed that positive Cs-atoms were emitted from a hot tungsten surface [6]. It has since become an important tool for producing ions partly due to relative simplicity and reliability of the needed equipment and stability of the ion charge state. The amount of required material is also low, even amounts less than 1μg are sufficient for surface ionization and the ratio of residual gases to the sample material is typically very advantageous. Surface ionization also makes the focusing of the beam simpler as the initial velocity distribution of the emitted ions is small, ionizing surface can be made equipotential and it's shape can be made to correspond to the focusing [46].

Though many processes lead to emission of ions from a surface of a solid body they can be divided into two groups [6]:

A Thermal equilibrium processes of ion emission from a surface
   1. Evaporation of ions of the emitter itself
   2. Desorption of any foreign particles temporarily adsorbed from the gaseous phase on the surface
   3. Desorption of foreign particles diffusing from the bulk of the emitter to the surface

B Thermal non equilibrium processes of stimulated ion emission from a surface
   1. Secondary ion emission
   2. Ion emission by the action of fast uncharged particles
   3. Electron-ion emission
   4. Photo desorption of ions
   5. Conversion and ionization of fast neutral particles

The difference between these two groups is that in the group A the particles stay on the surface long enough so that thermal equilibrium is achieved and that the

evaporation of particles takes place as a result of thermal excitation [6]. A strong dependence on temperature characterizes the thermal equilibrium processes. In these processes the energy distribution is Maxwellian with the distribution temperature equal to the temperature of the emitter. The processes in the group B are those where the non-Maxwellian particle energy distribution is formed by the interaction between the primary particles and the surface. All the above processes share one common property. As a particle leaves the emitter surface the initial quantum mechanical system, namely the particle-emitter system, gradually dissociates into an separate emitter system and a particle system. The particle flux from the surface contains neutral, negative and positively charged particles. From this it is possible to determine the degree of surface ionization α as a ratio of neutral atoms and ions of same kind. The basic principle of the surface ionization process is illustrated in figure 4.1. The most relevant factors affecting the degree of the surface ionization are the work function and the temperature of the surface material, and the ionization potential of the element to be ionized [46].

In the following treatment of surface ionization only the thermal equilibrium processes are relevant. The thermal equilibrium ion emissions fall into two categories depending on how the atoms to be ionized arrive on the emitter. If the atoms to be ionized are on the emitter or embedded into it the process is called the thermionic emission. In the case where the ions are thermally desorbed from an assembly of particles adsorbed on the surface of the emitter the process is called the surface ionization. Usually these two processes are labeled under the term surface ionization. In this following sections we study the surface ionization in the context of the WITCH off-line ion source. Also few other ionization methods are briefly presented.

4.1.1 Energy bands in surface ionization

In order to remove electron(s) from an atom and to ionize it one must overcome the binding energy of an atom on a ground state. Even for the outermost valence electrons this energy is several electron volts which means that in gaseous phase all substances are insulators as they do not have free electrons [6]. The ionization potential of individual atom ranges from 3.89 eV of cesium to 24.58 of helium [46]. As condensation takes place and the gaseous phase changes into solid phase, the atoms approach each other up to the equilibrium distance of the crystal lattice [6] and the potentials of individual atoms superpose into a single periodic potential $U(x) = U(x + L)$ of the crystal lattice.

In a solid the electrons are arranged in to energy bands which are separated by band gaps for which no wavelike electron orbitals exist [48]. The outmost energy band is called the valence band which can be either fully or partially occupied

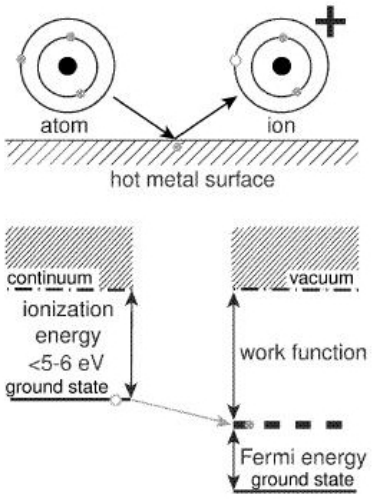

Figure 4.1: Illustration of the basic principle of the surface ionization process [47]

by electrons at T=0 K while all the inner bands are fully occupied. Usually in metals the outmost electrons are delocalized and can therefore move in the periodic potential of the lattice, in which they act very much like free electrons [49]. The energy of the valence band is represented at T=0 K by the Fermi energy E_0. From E_0 is possible to define the element specific work function $e\phi = E_m - E_0$ which is the energy that is required to separate an electron from the valence band. The E_m is a potential barrier of the surface of the solid [46], which is created by the electrons leaving the body and all the charged particles in the body [6]. One important aspect for band theory concerning the surface ionization phenomenon is the equilibrium distribution of valence electrons in the energy levels ϵ of the valence and conduction bands. This distribution is described by the Fermi-Dirac distribution [49]

$$f(\epsilon) = \frac{1}{e^{(\epsilon - E_0)/k_b T} + 1}. \tag{4.1}$$

The distribution 4.1 states the probability of finding an electron in an energy level ϵ at temperature T where k_b the Boltzmann constant. For example in the case of alkali metal the conduction band is also the valence band, but generally it differs whether the solid is a conductor, a semiconductor or an insulator.

4.1.2 Positive surface ionization from a homogenous surface

The degree of the surface ionization can be calculated by using the Nernst‘s [50] heat theorem[1]. It permits the calculation of the equilibrium constant C for a

1. Chemical reactions at a temperature of absolute zero take place with no change of entropy[51]

thermally equilibrated system at temperature T.

In the case of the surface ionization process the degreee of ionization is denoted as a ratio of charged particles to neutral particles [6]

$$\alpha_{\pm} = \frac{n_{\pm}}{n_0}, \tag{4.2}$$

where n_i, $i = 0, +, -$ are the densities of neutral, positive or negative particles. In a steady state the total density of the particles is the sum of the particle densities with different charge states $n=n_0+n_{\pm}$ which can be used to determine the ratio of the ion density to the total density

$$\beta_{\pm} = \frac{n_{\pm}}{n}. \tag{4.3}$$

The equilibrium constant can be calculated for $A \rightleftharpoons A^+ + e^-$ type reactions with equation [50]

$$C = \frac{n_e n_1}{n_0} = \left(\frac{2\sigma_1}{\sigma_0}\right) \left(2\pi m_e k_b T h^{-2}\right)^{3/2} exp\left(-W_1 (kT)^{-1}\right), \tag{4.4}$$

where W_1 is the ionization potential of the atoms, $\sigma_{1,0}$ are the statistical weights of the ionic and atomic ground states, m_e is the electrons mass, k_b is the Boltzmann constant and h is the Planck's constant. This equation was first calculated by J. Eggert for thermal plasma. In case of surface ionization the electron density n_{e0} at the ionizing surface comes from Richardson's law [50]

$$n_{e0} = 2\left(2\pi m_e k_b t h^{-2}\right)^{3/2} exp\left(-\phi (k_b T)^{-1}\right), \tag{4.5}$$

which gives the electron density at the surface. Here ϕ is the work function of the electron emitter. Inserting 4.5 to 4.4 gives [50]

$$\alpha = \frac{n_1}{n_0} = \left(\frac{\sigma_1}{\sigma_0}\right) exp\left[\left(\phi - W_1\right)(kT)^{-1}\right]. \tag{4.6}$$

A simple relation can be established between α and β by using eq's. 4.2 and 4.3 which yields

$$\beta = \frac{\alpha}{1+\alpha}. \tag{4.7}$$

The equation 4.7 is known as the Langmuir equation and it gives the surface ionization efficiency as a function of T. It is also possible to express the degree of ionization for positive particles with the help of the isothermal heat of evaporation l. A thorough derivation of the equation

$$\alpha = \frac{\nu_+}{\nu_0} = \frac{C}{D} e^{\frac{l_0 - l_+}{kT}}, \tag{4.8}$$

via kinetic equations for the desorption is done in [6]. In the equation 4.8 the C and D are temperature dependent coefficients and

$$\nu_i = NCe^{-\frac{l_i}{kT}}, \tag{4.9}$$

where i=+,0 are the particle fluxes for positively charged and neutral particles and N is the surface concentration of particles.

The previous examination is made with the assumptions that the surface on which the ionization takes place is homogenous and the whole process takes place in a thermal equilibrium. Also the effects of a possible external electric field and the possibility of varying work function were neglected. These additional assumptions modify the degree of the surface ionization to some extent but the examination of this is out of scope for this thesis.

4.1.3 Thermal ionization

In the beginning of this chapter, the thermal emission was examined as a process in which the ions are emitted from the emitter material and from the surface impurities contained in it [6]. As in the previous section a thermal equilibrium is assumed but in this case for a vapor above a metal surface. The vapor consists of neutral and charged ions and it is assumed to have pressure low enough for the laws of ideal gas to apply. With these premises and by assuming that the particles are not reflected from the surface, the fluxes of particles from the surface are related to the equilibrium vapor pressure by

$$\nu = \frac{p}{\sqrt{2\pi M k_b T}}, \tag{4.10}$$

where p is the vapor pressure, M is the particle mass, T is the temperature and k_b is the Boltzmann constant. The assumption of the negligible reflection is good as the reflection factor has been measured to be zero for some alkali metal atoms including K and it's also zero for all metals with high probability [46]. The flux of the ions with different charge states can be derived from the Clausius-Clapeyron equation

$$-l(T) = k\frac{dln(p)}{d\left(\frac{1}{T}\right)}. \tag{4.11}$$

l(T) in this equation is the isothermal heat of evaporation in a system with non-zero electric field and non-zero surface coverage [6]. Now the sublimation energy

for the ions with different charge states can be expressed by

$$l_i(T) = \frac{-\gamma dln(\nu_i\sqrt{T})}{\left(\frac{1}{T}\right)}, \tag{4.12}$$

where γ is independent of the temperature and i=+, - or 0 depending of the charge of the ion. As was the case with the surface ionization the degree of ionization for thermal ionization can also be denoted by the ratio of the fluxes of neutral and charged particles. By using eq. 4.8 and using Schottky's formula $l_{00} - l_{0+} = e(\phi - V)$ the degree in the case of thermal ionization becomes[6]

$$\alpha_+ = \frac{\nu_+}{\nu_0} = \frac{C}{D} e^{\frac{\phi - V}{kT}} \tag{4.13}$$

for positive ionization where ϕ is the work function of the electron emitter and V is the ionization potential of the atom.

Both the REX-TRAP ion source and the WITCH ion source produces ions from an emitter that is made of aluminosilicate zeolite. These kind of thermionic emission of complex composition includes also the Kunsman and Koch emitters which use iron catalyst and tungsten powder - alkali-halide mixtures to produce ion currents. Ion sources utilizing zeolite to produce ions typically produce very stable ion beams [6].

4.2 Other ionization methods

4.2.1 Resonant laser ionization

Resonant laser ionization or RILIS, produces positive ions by removing electrons from atoms by focusing a intense beam of light onto the substance to be ionized (see Fig. 4.2(a)). Currently this kind of ion sources are operating for example at ISOLDE at CERN and at TIARA in Takasaki.

The ionization is done by exiting the atoms valence electrons with resonant photons absorb so that eventually the electron is removed from the atom [47]. A few excitation schemes for different elements are presented in figure 4.2(b). Laser ionization can ionize elements that cannot be ionized via surface or electron impact ionization and it has already been applied to elements with ionization energies up to 9 eV [53]. The resonant laser ionization can also be tuned to be not only element sensitive but also isotope selective in heavy elements because of isotope shift, or isomer selective by taking advantage of hyperfine splitting. Laser ionization is also suspectible to the fine structure of atoms, which can cause reduction

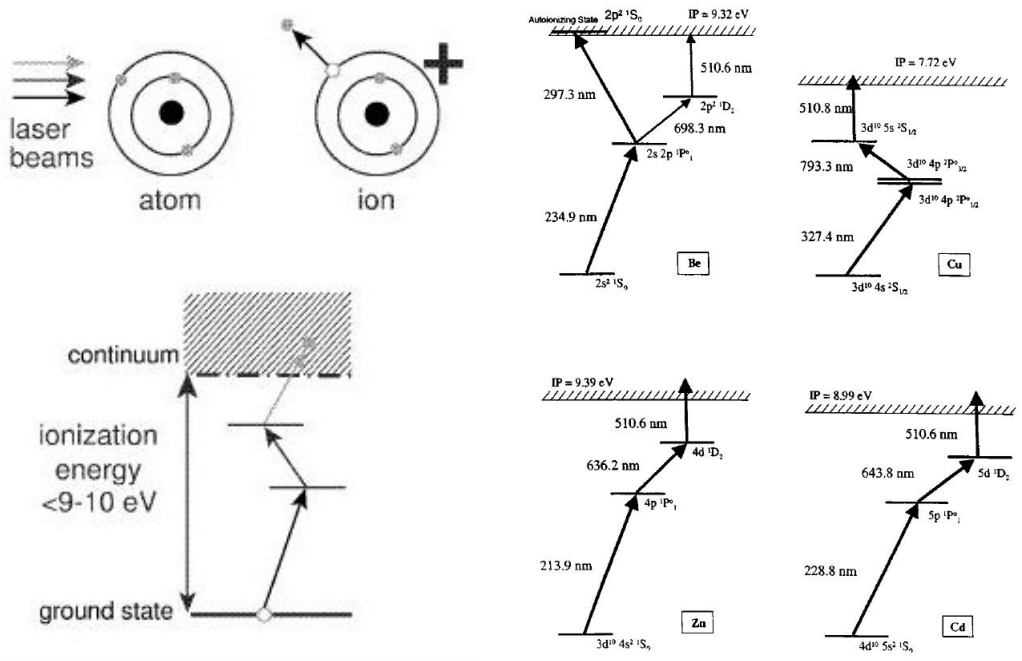

(a) (b)

Figure 4.2: Illustration of the basic principle of the laser ionization [47] (a) and excitation schemes for resonant laser ionization for Be, Zn, Cu and Cd [52] (b).

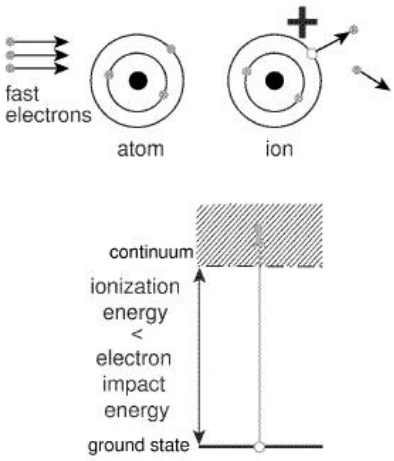

Figure 4.3: Illustration of the basic principle of the electron impact ionization [47]

in ionization efficiency, and nuclear polarization in which the circular polarization of the laser light is transmitted into the excited state of the atom.

Resonant laser ionization sources can be divided into hot cavity -, buffer gas cell - and pulsed desorption -ion sources [47]. In the hot cavity set-up the laser light is focused through a small outlet hole in to a cavity holding the atoms to be ionized. As the atoms stay in the cavity only about 0.1 ms the ionizating laser has to have high repetition rate, typically 10 kHz, in order to ensure that each atom interacts with the laser. Currently this rate is achieved by using copper vapor lasers providing several 10 W beams with 511 nm - 578 nm wavelength to a dye laser which are used to increase the wavelength spectrum range to 210nm - 1000nm scale. In the simplest case the ionizer cavity is identical to the surface ionization tube. The tube is made for example of tungsten to allow temperatures up to 2000°. This heating ensures that the laser ionized beams consists solely of atomic ions but it also causes troubles as it enables surface ionization in the target [47]. This requires special steps to either cool the cavity by separating it from the material to be ionized or by suppressing the isobaric background. The suppression is done for example by applying a strong longitudal electric field into the cavity which effectively cuts out the beam resulting from surface ionization by gating the electric field on to the short bunches of the ions [53].

4.2.2 Electron impact ionization

In order to produce either positive or negative ions one needs either to add or remove an electron from an atom. To remove electron(s) from the atom, assuming that the electrons are ejected from the outmost layer of the atom/ion , and to

produce a positively charged atom, one can bombard the atom with electrons to achieve a reaction (see Fig. 4.3)

$$e + X \longrightarrow X^+ + 2e \tag{4.14}$$

for a singly-charged ion or

$$e + X^{i+} \longrightarrow X^{(i+1)+} + 2e \tag{4.15}$$

for multiple-charged ions [54]. In a system where atoms are bombarded with electrons the charge state evolution can be expressed by

$$\frac{dn_0}{dt} = n_0 \sigma_{0,1} j_e \tag{4.16}$$

and

$$\frac{dn_i}{dt} = n_{i-1}\sigma_{i-1,i} j_e - n_1 \sigma_{i,i+1} j_e - \frac{n_i}{\tau_c(i)}, \tag{4.17}$$

where n_0 is the neutral particle density, n_i is the charged particle density, $\sigma_{i-1,i}$ is the cross-section for single step ionization for charge state i, j_e is the electron current density and $\tau_c(i)$ is the life time of the ion in a charge state i without ionization [54]. The positive electron impact ion source can either produce high current of singly charged ions or low current of multiply-charged ions or any combination in between.

The production of negative ions via electron impact, or more precisely volume processes by electron impact, can be separated into three reaction types[54]: dissociative attachment, polar dissociative attachment and dissociative recombination. In dissociative attachment slow electrons are stably attached to atoms during their interactions with (exited) neutral molecules according to the reaction

$$e + XY \longrightarrow X^+ + Y. \tag{4.18}$$

The polar dissociative attachment means that the slow electron is not captured but it excites the molecule into an unstable state via the reaction

$$e + XY \longrightarrow X^+ + Y^-, \tag{4.19}$$

and the dissociative recombination means that negative ions are formed when electrons collide with a positive molecule

$$e + XY^+ \longrightarrow X^+ + Y^-. \tag{4.20}$$

Different kinds of ion source constructs have been built to take advantages of these reactions in order to produce ions with a wanted charge state. Main types of positive ions sources that utilize electron impact ionization are separated into groups by their ion production properties. Here are a few examples of the ion sources in different categories.

- High current- singly charged ions
  - Filament ion source
  - Microwave ion source
  - Metal vacuum arc (MEVVA) ion source
- Multiply charged ions
  - Duoplasmatron ion source
  - Penning ion gauge (PIG) ion source
- Low current- high charge state
  - EBIS
  - ECR

Ion sources like PIG can produce charge states up to +10 but high charge state ion sources as EBIS and ECR ion sources can produce charge states up to +25 [54]. For example, an EBIS ion source is installed at the REX-ISOLDE experiment as a charge breeder to increase the charge state of the radioactive ions in a very short time period [53]. Volume produced negative ions sources include so called classical negative ions source and multi-cusp negative ions sources [54]. The positive electron impact ion sources are mostly used to produce highly charged positive ion beams while the negative sources are used to produce negatively charged hydrogen or heavier ions to be used in accelerators.

The working principle and construction of electron impact ion sources are usually more complex than surface ionizing ion sources. For example the EBIS working principle can be divided into five parts [55]:

1. A electron beam with wanted parameters is produced.
2. A electrostatic ion trap is generated inside the ion source.
3. Neutral particles or ions with low charge state are injected into the ion trap during a suitable time frame.
4. The ions are stored inside the trap until the wanted charge state has been achieved.
5. Extraction of ions.

The EBIS produces pulsed ion bunches with a very precisely defined charge state for each ion.

4.3 Beam shape analysis

The measurement of the beam shape is done by either moving a detector across the beam or by moving a collimator in front of the beam so that a part of the beam is blocked. In the case of moving a Faraday cup or a collimator across the beam the geometrical situation is the same. To extract the actual beam width from the measurement data one must do a following geometrical examination of the measurement situation. To simplify the situation it is assumed that the beam is smaller than the Faraday cup and that the beam and the cup are on the same x-axis. Figure 4.4 shows the situation when the beam is completely inside the Faraday cup in two positions. The symbol Y is the distance between the beam center points while the beam is still inside the Faraday cup, R is the beam diameter and D is the diameter of the Faraday cup. From this it can be easily seen that the beam diameter R is

$$R = D - Y. \tag{4.21}$$

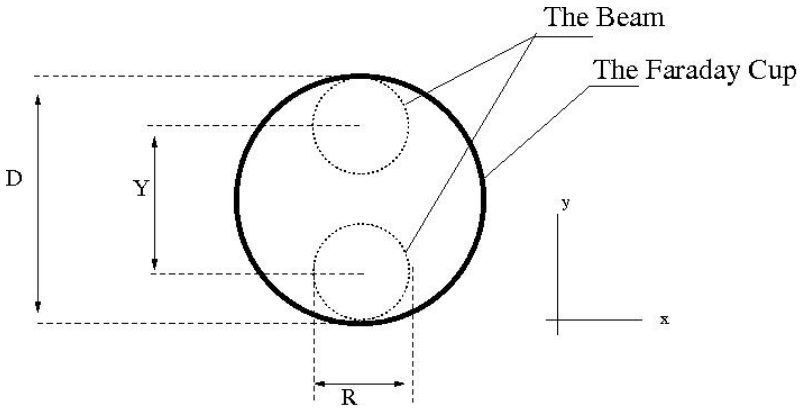

Figure 4.4: Illustration of the geometry involved in the beam width measurements

If the beam is larger than the Faraday cup the equation 4.21 changes into

$$R = D + Y. \tag{4.22}$$

These equations also hold for circular collimators with the exception that now the equation 4.22 holds when the beam is smaller than the circular hole in the collimator and vice versa. Errors for these equations can be calculated by using the equation for error propagation [56]

$$\delta F(x_1, ..., x_n) = \sqrt{\sum_i^n \left[\frac{\partial F}{\partial x_i}\delta x_i\right]^2}, \tag{4.23}$$

where F is the function, $\frac{\partial F}{\partial x_i}$ are partial derivatives for each measurable component and δx_i is the error of the corresponding component. Now the error for the beam diameter gets a form of

$$\delta R = \sqrt{(\delta D)^2 + (\delta Y)^2}. \tag{4.24}$$

If the beam diameter is measured to be different in two perpendicular directions one can approximate those diameters to correspond to be the minor and major axis of an ellipse. The length of the axis can be deducted with the equations described before so that no big error is made if the beam is only slightly elliptical.

The collimator strip included a 20×1 mm^2 rectangular slit which requires a different approach. The slit is wide enough to cover the whole Faraday cup diameter so at every position the slit allows a 1 mm wide and at maximum 16.5 mm long strip of ions to pass in to the cup. To find out the area of this strip, one must calculate the area of intersection for two different circular segments [57] with a constant difference in height $l = 1$mm. The geometry involving a circular segment is presented in figure 4.5 in circle no. 1.

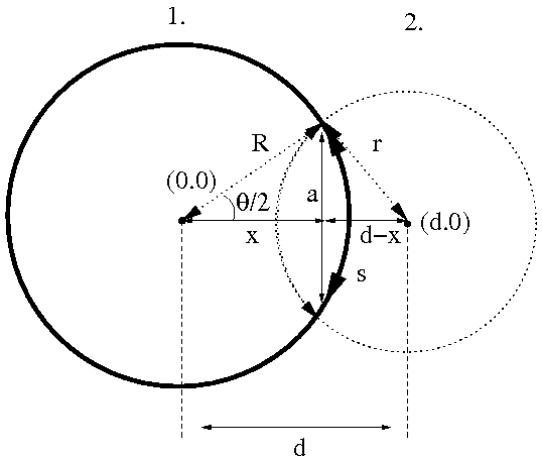

Figure 4.5: A Circle-Circle intersection

By selecting the center point of the slit to be d_x=x which is also the height of the segment (see Fig. 4.5) the area for a circular segment can be obtained with

equation

$$
\begin{aligned}
A_x = & \int_{-\sqrt{R^2-d_x^2}}^{\sqrt{R^2-d_x^2}} \int_{d_x}^{\sqrt{R^2-x^2}} dydx = \\
& \int_{-\sqrt{R^2-d_x^2}}^{\sqrt{R^2-d_x^2}} \sqrt{R^2-x^2} - d_x \, dx = \\
& R^2 \tan^{-1}\left(\frac{\sqrt{R^2-d_x^2}}{d_x}\right) - d_x\sqrt{R^2-d_x^2}.
\end{aligned}
\tag{4.25}
$$

The intersection area of two circular segments is obtained by taking a subtraction of d_u=d_c+l/2 and d_l=d_c-l/2 which yields

$$
\begin{aligned}
\Delta A_s = & R^2 \tan^{-1}\left(\frac{\sqrt{R^2-(d_c-1/2)^2}}{d_c-1/2}\right) \\
& - R^2 \tan^{-1}\left(\frac{\sqrt{R^2-d_c+1/2^2}}{d_c+1/2}\right) \\
& - d_l\sqrt{R^2-(d_c-1/2)^2} + d_u\sqrt{R^2-(d_c+1/2)^2},
\end{aligned}
\tag{4.26}
$$

where d_c is the center point of the slit. The equation 4.26 is valid when $d_c \in [1/2, r-1/2]$. The equation 4.25 also works for finding the area for two intersecting circles which would represent a situation where the beam is scanned with the Faraday cup. The area is obtained by adding the areas of the circular segments of the two circles 1 and 2 (see Fig. 4.5). To get the height of both segments one must solve the intersection points for the circles 1. and 2. and the length of the chord a by simultaneously solving [58]

$$
\begin{cases} R^2 = x^2 + y^2 \\ r^2 = (x+d)^2 + y^2 \end{cases}, \tag{4.27}
$$

which gives

$$
x = \frac{d^2 - r^2 + R^2}{2d}. \tag{4.28}
$$

By inserting eq. 4.28 back to eq. 4.27 and solving y, one can obtain $a = 2y$ by using Pythagoras theorem which gives

$$
a = \frac{1}{d}\sqrt{4d^2R^2 - (d^2 - r^2 + R^2)^2}. \tag{4.29}
$$

Now by choosing d_1=x=$\frac{d^2-r^2+R^2}{2d}$ and d_2=d-x=$\frac{d^2+r^2-R^2}{2d}$ to be the heights of the two segments and noticing that the $\phi = \frac{s}{R}$ which can also be presented as $cos^{-1}\left(\frac{d_x}{R}\right)$ and further as $\tan^{-1}\left(\frac{\sqrt{R^2-d_x^2}}{d_x}\right)$, one gets the area of intersection as

$$\begin{aligned}\Delta A_l = r^2 cos^{-1}\left(\frac{d^2+r^2-R^2}{2dr}\right) + R^2 cos^{-1}\left(\frac{d^2-r^2+R^2}{2dR}\right) \\ - \frac{1}{2}\sqrt{4d^2R^2-(d^2-r^2+R^2)^2},\end{aligned} \tag{4.30}$$

which is valid when d$\in [R-r, R+r]$

By assuming a beam that's current density is constant over the whole beam area in addition to the assumptions stated in the beginning of this section, one can calculate the flux of ions at the detector as a function of the position of the Faraday cup or of the collimator. Now when using equations 4.30 and 4.26 one can get a picture of what kind of results the measurements yield if the beam fulfills the assumptions stated in this section. The figure 4.6(a) shows the simulated results for a beam scan made with a Faraday cup with a diameter of 16.5 mm where

$$\begin{cases} 0 & d > 11.75mm \\ \Delta A_l & d \in [5.5mm, 11.75mm] \\ 4/3\pi(3.25mm)^3 & d < 5.5mm. \end{cases} \tag{4.31}$$

The beam diameter is assumed to be 6.5 mm and the figure 4.6 shows the simulated results for beam scan with a $20\times1\text{mm}^2$ collimator slit for a beam with a diameter of 16 mm where

$$\begin{cases} 0 & d_c > 8.75mm \\ \Delta A_s & d_c \in [0.5mm, 8mm]. \end{cases} \tag{4.32}$$

The assumptions in the previous examination do not take into account the possibility that the beam is elliptical or that the Faraday cup or the collimator holes and the beam do not move along the same central axis. Also the beam intensity is assumed to be constant over the whole beam area and it's assumed that even if these sort of error sources are present their effect is negligible.

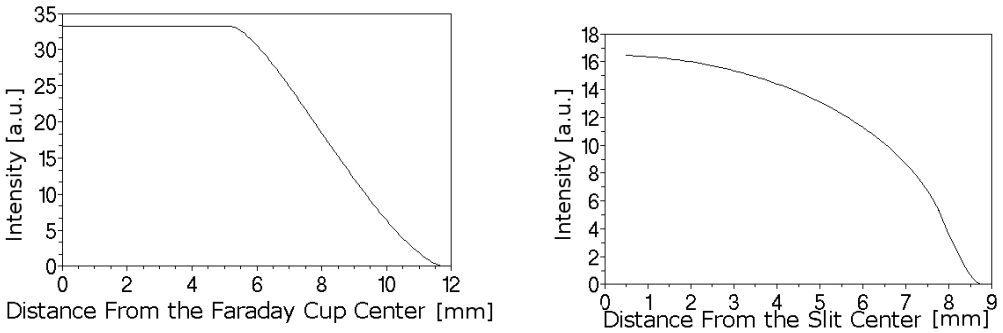

(a) (b)

Figure 4.6: Simulated beam width measurements using a Faraday cup (a) and a rectangular collimator (b). [a.u.] = arbitary units

Chapter 5

Ion sources for WITCH set-up off-line tuning

Currently the WITCH experiment beamlines, the spectrometer and the Penning traps etc. are tuned off-line with the REX-TRAP ion source or with a small crossbeam ion source by Pfeiffer [59]. The on-line tuning could be used to tune the set-up for a specific radioactive ion, but it might deposit radioactive background to the MCP and to other parts of the set-up. Also in addition the available beamtime is very scarce so that better to use it to run real experiment and to tune the WITCH set-up off-line.

The Pfeiffer cross-beam ion source is located in the VBL to be used to tune the Penning traps and the retardation spectrometer. The cross-beam ion source means that the gas jet, electron beam and the ion extraction are mutually perpendicular. This construct combined with thin sheet metal construction prevents the wall interactions of the gas jet almost completely and allows the ion source interior temperatures rise up to 200°C which prevents vapor condensation [59]. The Pfeiffer ion source works by accelerating electrons, emitted from a heated tungsten filament, to 70 eV and guiding them into a ionization chamber where they ionize gas. The ionized atoms are extracted with an extraction electrode and focused with an ion lens which has been modified so that it can produce a pulsed beam [9]. Electrode configuration and potential characteristics of the Pfeiffer ion source are presented in figure 5.1. The gas is injected in to the ionization chamber from outside of the VBL and the ion source is mounted on a sliding support so that it can be moved in when needed. The ion source can achieve beam intensities up to 100 nA [2] when suitable cathode current and gas pressure are applied.

The REX-TRAP ion source is not the most optimal solution for acquiring stable ions for off-line tuning of WITCH because the ion source is not always available as it is also used by other experiments. Likewise the Pfeiffer ion source can only produce 100 eV ions so it cannot be used to real experiment even if mounted to the beginning of the beamlines. For these reasons a new 60 keV ion source was needed that would be mounted directly to the HBL of the WITCH set-up and

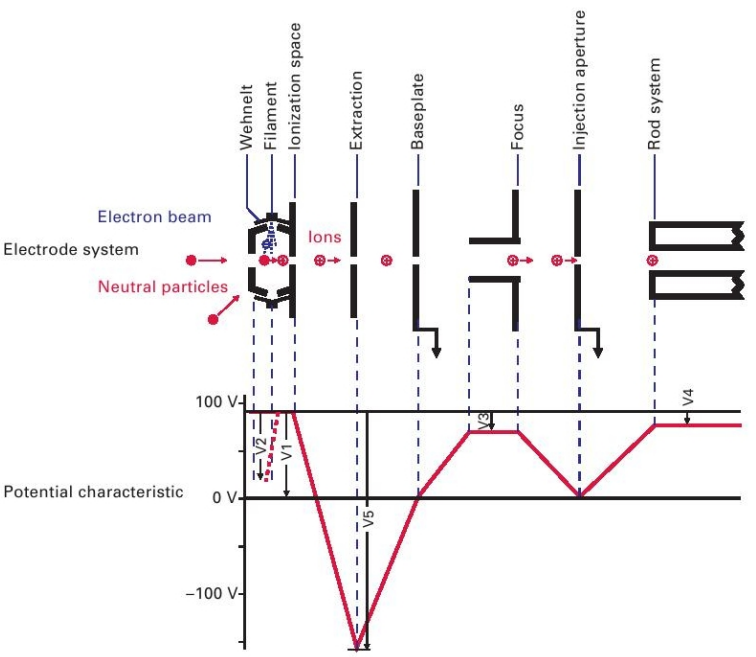

Figure 5.1: The Pfeiffer cross-beam ion source structure [59]

which would be available on demand for off-line tuning [9]. This new ion source will not replace the REX-TRAP ion source but it will be used as a complementary ion source at times when the REX-TRAP is not available.

5.1 REX-TRAP and WITCH off-line ion sources

The main off-line ion source used by the WITCH experiment is the REX-TRAP ion source (see Fig. C.4). The ion source design is almost identical with the WITCH ion source, which both are surface ionizing ion sources designed to produce 30 keV to 60 keV alkali-ions with ion current up to few nA [35].

The ion source construct consists (see Fig. 5.1) of two main parts, a high voltage base flange, to which the ionizing unit and the exraction electrode are attached, and an extraction lens. The base flange and the vacuum chamber are separated by an insulator so that the extraction lens is at the ground potential and for security reasons the whole high voltage (HV) part is inside a Faraday cage. The zeolite that is to be ionized is placed in a conical graphite cylinder. This is heated by an electric current which causes the front of the cylinder to be in the highest temperature. The front of the cylinder also has tungsten filaments to aid the ionization process. Depending on the zeolite the ion source can produce ion beams of $^{133}Cs^{+}$, $^{39}K^{+}$

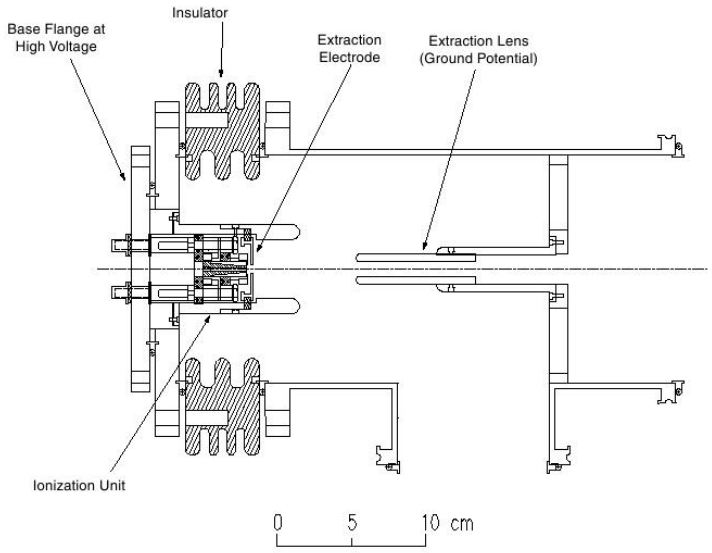

Figure 5.2: The REX-TRAP/WITCH ion source design [35]

and $^{23}Na^{+}$ with a emittance of about $10\pi \cdot mm \cdot mrad$ (REX-TRAP ion source). For example currently the WITCH ion source produces Potassium ions (K^{+}) which are ionized from a potassium alumina silica zeolite e.g. $K_20 \cdot Al_2O_3 \cdot 4SiO_2$ [60].

5.2 The WITCH ion source

The WITCH ion source (see Fig. 5.3) was designed and made at IKS[1] in Leuven Catholic university. The ion source chamber and the bender chamber are the main sections of the ion source. The ion source chamber contains the actual ion source and the extraction electrodes. The bender chamber holds the bender which is made of two spherical electrodes with radiuses of 180 mm and 200 mm. The bender is used to guide the ions from the vertically placed ion source chamber to the HBL of the WITCH set-up. The ion source was first assembled to a test set-up and later it was installed permanently to the HBL.

5.2.1 Assembly

The ion source parts were shipped to CERN from IKS along with the vacuum system, the power system and with some cages, shielding tubes and diagnostics

1. Instituut voor Kern- & Stralingsfysica

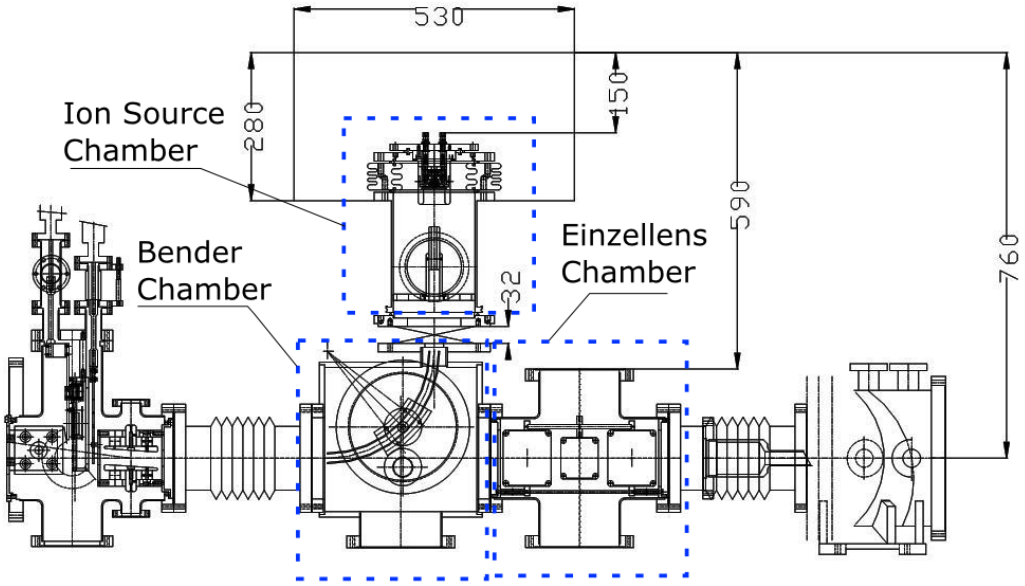

Figure 5.3: The complete WITCH ion source in it's final configuration in the HBL.

equipment. Additional parts such as copper rings were acquired from CERN. At first the ion source was assembled to a test set-up which meant that it had extra diagnostics chamber and blind flanges which would not be present in the final configuration. For practical reasons the ion source was partially dissassembled to ease transportation and installation into the HBL for the final set-up. In this section the word ion source refers to the ion source set-up as a whole (see Fig. C.1(a)) unless otherwise stated. Explanations for the numbers in figures 5.4 and 5.5 are presented alongside the figures and the numbers will be used from now on in this section when referring to a certain part of the ion source.

The assembly of the ion source test set-up concentrated on the bender chamber (5) to which almost all the other parts were mounted. The bender flange (1) holds a sliding feedthrough made by Caburn-MDC and the connectors for the bender. The feedthrough allows the bender to be moved in when needed. The diagnostics tube (2) contains a Faraday cup, namely the Faraday cup 1, which is mounted on a MDC made linear feedthrough(4). The connectors for Faraday cup 1 are on flange number 3. The Faraday cup 2 was mounted on a flange opposite the bender flange so that the cup was directly under the ion source chamber (7). The ion source chamber (7) was connected to the bender chamber (see Fig. C.3(b)) (5) with a valve (12) so that the two chambers could be separated for maintenance

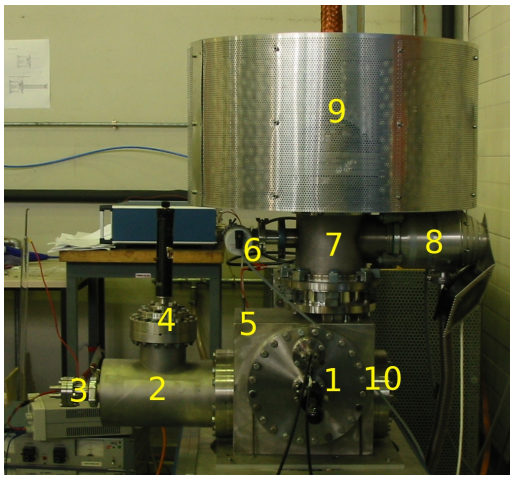

1. Bender flange and sliding feedthrough
2. Diagnostics tube
3. Faraday cup 1 connectors
4. Faraday cup 1 linear feedthrough
5. Bender chamber
6. Vacuum gauge and a venting valve
7. Ion source chamber
8. Turbo-pump
9. Faraday cage
10. Back blind flange

Figure 5.4: A side view of the ion source test set-up from the bender control side

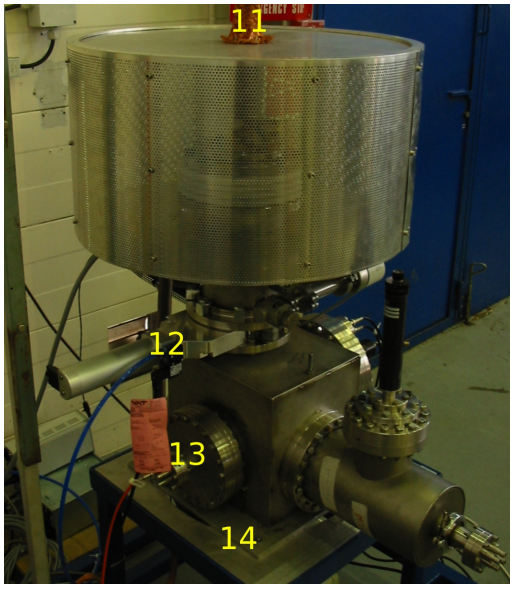

11. HV cable tube
12. Valve
13. Faraday cup 2 flange
14. Bottom blind flange

Figure 5.5: A side view of the ion source test set-up from the valve side

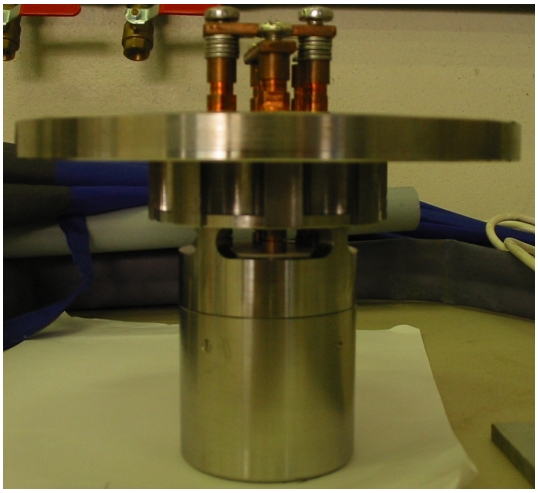

Figure 5.6: The actual ion source [61]

purposes. Also for this purpose a turbo-pump (8) and a gauge (6) was connected to the ion source chamber. The ion source itself (see Fig's. 5.6 and 5.7) was mounted on the top of the ion source chamber on a high voltage platform inside the Faraday cage (9) and blind flanges were mounted on the remaining holes (10) and (14). All the flanges, the turbo-pump and the other equipment were sealed with either copper seals or rubber seals to ensure high vacuum.

A tube containing the high voltage cables was constructed to shield these cables as they had to be drawn from the high voltage system to the ion source. The tube was first made of two nested transparent elastic PVC tubes with a copper threading on the outside. This construct turned out to be problematic as it charged and produced sparks at 30 kV which is the lowest accepted voltage for the ion source operation. The charging also manifested itself as a very high leakage current (up to few μA) at the HV source which could have caused damage to the equipment. For this reason the flexible PVC tubes were replaced with a single layered rigid and opaque PVC tube with the copper threading. This way the test set-up could reach the 30 kV voltage without sparking and without any significant leak current. The same tube type was used to construct the HV tube for the final set-up.

The high voltage system which provides the ion acceleration, the heating current and the extraction voltage is basically the same in the test set-up and in the final set-up. During first start up test in the test set-up the HV system had the external power regulation implemented but it malfunctioned, which caused the heating power to rise as from the pre-set level. The power regulation was re-implemented for the final set-up but even though it was remade at IKS it still malfunctioned for which it was bypassed.

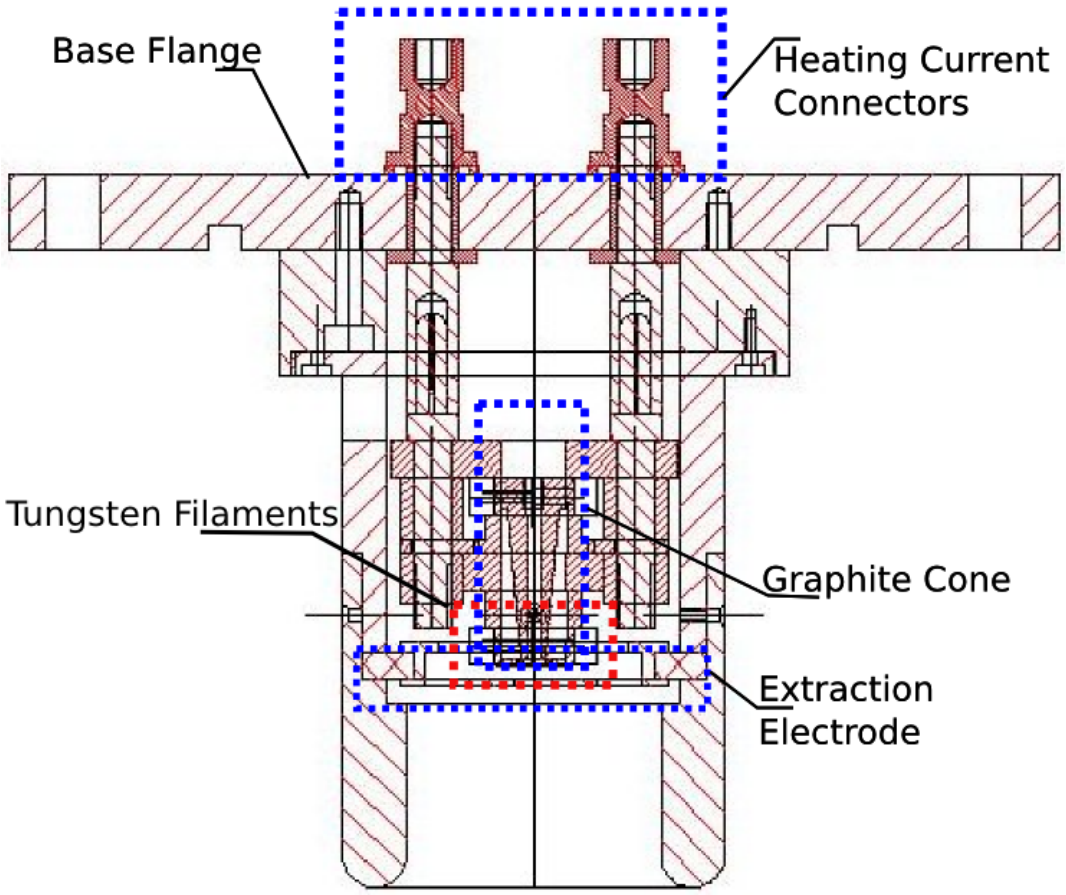

Figure 5.7: Schematic view of the actual ion source

The malfunctioning electronics prevented the external heatin current current control which meant that the system had to be managed manually. For this the HV system had to be powered down when the heating current needed to be adjustement. This caused practical problems and problems with the measurements.

The WITCH HBL (see Fig. 3.3) had to be slightly altered before the ion source could be installed to it. The chamber after the Einzel lens was removed, the high voltage feed into the Einzel lens was rotated 90° and a 600 L Alcatel turbo-pump was installed on the Einzel lens chamber to provide vacuum to the HBL. The ion source itself in the HBL was in exactly the same assembly as it was in the test set-up except that the diagnostics tube and the back blind flange were removed along with the bottom blind flange. The installation prodecure began by mounting the bender chamber to the Einzel lens chamber after which the ion source chamber was mounted on top of the bender chamber along with the bottom plate of the Faraday cage. The rest of the Faraday cage was installed after this along with a valve to cover the bottom of the bender chamber. This multi-step installation was done partly because of space constraints imposed by the WITCH platform (see Fig. C.1(b)).

5.2.2 Ion source set-up

Ion source (see Fig. 5.3) set-up consists mainly of the following sections: the ion source, high voltage system, measurement equipment and vacuum systems. In this section the ion source refers to the whole system including the ion source, ion source chamber and bender chamber. The set-up scheme is presented in figure 5.8. The parts indicated by 1 to 4 in this figure are located inside the Faraday cage and all equipment in there but the transformer are on a high voltage platform (see Fig. C.2(c)). The connections for the ion source HV part and for the Faraday cups and the bender are presented in figures 5.10 and 5.11.

5.2.3 Ion source startup

Ion source startup is a slow process due to the fact that too fast ramping of heating current and HV might damage the equipment. This means that it takes about half an hour to get the the heating current up to about 25 A. As the set-up lacks the power regulation it needs about an hour stabilization time before the ion current is stable enough. The start-up prodecure described in table 5.1 is the same for the final set-up and for the test set-up.

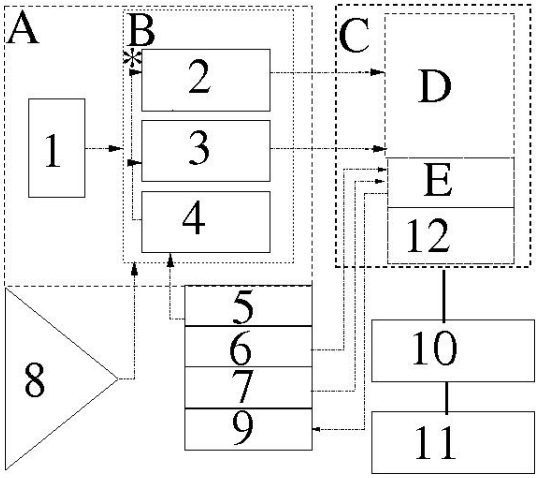

Figure 5.8: Ion source set-up power feeding scheme and vacuum system.

1. Transformer Mosef-Glasev (see fig.C.2(a))
2. Power source Xantrex EMV XPD 7.5-6.7
3. Extraction voltage supply
4. Xantrex Bertan optical Va controller
5. LV optical Va controller
6. Hewlett Packard E3612A DC power supply (IKS power supply)
7. Bender power supply
8. FVG HCN 6.5-65000 high voltage power supply
9. Keithley 6512 programmable electrometer
10. Alcatel Pre vacuum pump
11. Alcatel ATP 150 Turbo-pump and ACT 600T Control unit
12. Valve VAT N-6288-213 and Pfeiffer vacuum compact full range gauge

A Faraday cage. Connections inside the Faraday cage are presented in fig 5.9.

B High voltage platform

C Ion source

D Ion source Faraday cage

E Ion source chamber and diagnostics

$*$ Power regulation cable. Presently not connected

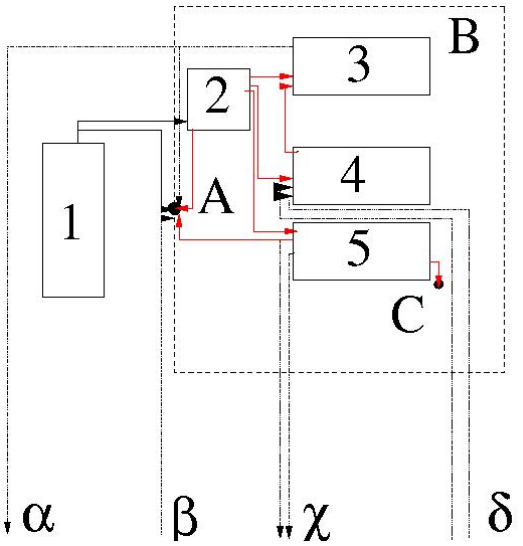

Figure 5.9: Details of the HV connections for both test and final set-up.

1. Transformer Mosef-Glasev
2. Power outlet
3. Extraction voltage supply
4. Xantrex Bertan optical Va controller (SET → IN at 3)
5. Power source Xantrex EMV XPD 7.5-6.7

A & C Grounding points to the HV platform.

B HV platform (see Fig. C.2(b))

α Coaxial cable to the ion source

β HV voltage from FVG HCN 6.5-65000 high voltage power supply

χ Heating current to the ion source. Negative busbar is ground

δ Optical fibers from LV optical Va controller (P_xSET,V_BSET → P_xSET,V_BSET)

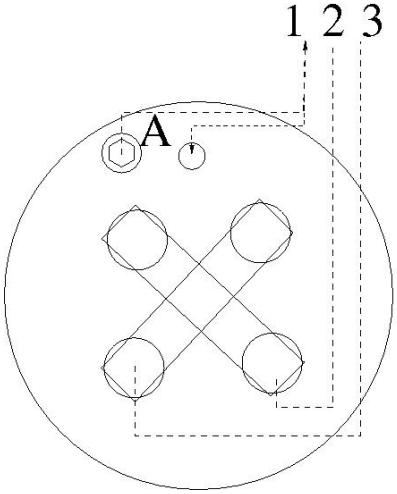

Figure 5.10: Ion source high voltage base flange connections

1. Coaxial cable to the extraction voltage supply

2. & 3. Heating current cables to the Xantrex power source

A Coaxial cable ground

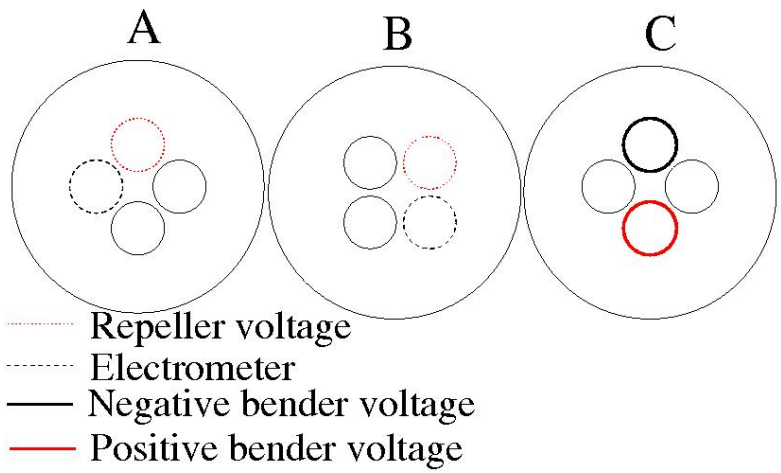

Figure 5.11: Connections for the Faraday cups, the repeller and the bender. Faraday cup 1 (A), Farady cup 2 (B) and connectors for the bender (C)

Table 5.1: The WITCH ion source start-up prodecure. The numbers in brackets are explained in figure 5.8

1. Check that the vacuum (12) inside the ion source is good ($10^{-7} - 10^{-6}$ mbar) and that the valve (12) is open. The valve is open when it's powered.
2. Connect the transformer(1) to a normal 220V socket.
3. Turn on the controller (4), extraction voltage supply (3),LV optical controller (5) and the heating power supply (2).
4. Increase the heating current to the wanted value from the optical controller. This must be done in 2 A steps with at least 30 second intervals.
5. Close the HV cage with at least three nuts, from the top middle and from the middle of both sides.
6. Raise the high voltage supply (8) to 30 kV slow enough that the leakage current stays well below 1 μA and that the green warning light above the current control does not light.
7. Check that the bender is in before powering the bender power source (7). This is because if the bender is out, the other bender plate is connected to the ion source chamber.
8. Set the repeller voltage (6) to 100 V.

Chapter 6

Measurements and results

The measurements made with the WITCH ion source test set-up were made with a rather limited number of diagnostics tools and tunable parameters. The diagnostics equipment at the test set-up allowed the measurement of the beam intensity and shape in horizontal x-direction and vertical y-direction as a function of bender voltage and extraction voltage when measuring after the bender. The the beam intensity was the only tunable parameter when measuring the beam straight from the ion source. After the ion source was installed into the HBL it became possible to use also collimators and MCP's to monitor the beam, and to use the kicker, steerer and bender electrodes in the HBL to manipulate the beam.

The bender voltages for the test set-up were deducted straight from the reading on the IKS bender power source by multiplying this number by 10. This causes an error of a few percent (see Fig. A.1) on the operating voltages which can however be considered to be insignificant in the context of these measurements. The bender voltage source was changed from a source marked '7-8' to a source marked '5-6' (see figure 5.8 item 7) after the current stabilisation measurement for I_H= 25.7. In the final set-up the bender voltages were provided by a power source that was controlled by LabVIEW® based software. The software was also used to control the HBL electrode voltages.

Measurements for both set-ups suffered from the lack of power regulation which caused the ion current intensity to fluctuate and behave unstable. This in turn made the comparison of ion currents between different measurements impossible. The maximum power to be allowed during measurements was limited to be about 35 W and it had to be solved manually from the heating current I_H and the heating voltage V_H with the equation $P = V_H \cdot I_H$.

During the final set-up test's it was noticed that the tube connecting the turbo-pump to the ion source chamber had a leak on the welding which caused the vacuum inside the HBL to be around $1{\cdot}10^{-7}$ mbar instead of the normal $1{\cdot}10^{-8}$

mbar.

6.1 Beam current stabilization

Measurement configuration

After the ion source has been powered up it takes some time to get the ion beam current I_i sufficiently stabilized. This time was measured several times for different heating currents I_H and extraction voltages V_E from both sides of the bender, in the test set-up and in the final set-up. The point after which the current was considered to be stabilized was very subjective. The beam current never stabilized completely so the timing was stopped when the change in the ion current was deemed to be slow enough for other measurements.

The measurements were done with a timer and with an electrometer (see figure 5.8 item 9) that was connected either to the Faraday cup 1 or 2. Timing was started after the electrometer indicated a beam coming from the ion source. The ion current was logged every 1-10 minutes depending on the measurement and the rate with which the ion current changed. The values were logged more frequently if the rate of the ion current change was high. If the the measurements were done after the bender, the bender voltages $V_{\pm B}$ were set to values which were known to yield the good transport efficiency through the bender.

The ion source configurations used in the test are described in table 6.1. The measurements spanned over a long period of time. This means that the stabilization curves measured during different sessions cannot be used to compare the ion currents achieved with each configuration. Also the fact that the extraction voltage changed between sessions makes any comparison impossible. At best the differences between the maximum ion current and the stabilized ion current can be compared. This was done by taking the peak intensity and approximating the stabilized intensity from the ion current stability graphs (6.1) for each measurement. The information yield from this is quite minimal but it can still be used to approximate how much the lack of power control decreases the maintainable ion current. Some of the measurements also include the information of the heating power change during the stabilization period. This meant that the heating current U_H had to be read from the heating power source (see figure 5.8 item 2)

Results

Figure 6.1 shows the evolution of the ion source current with time during about 1 hour from the moment the ion source is in full operation. The configurations

Table 6.1: Ion source configurations for ion current stability measurements. Measurements 9 and 10 were made in the final set-up. I_H=Heating current , V_E=extraction voltage, $V_{\pm B}$= bender voltages, F.Cup= Faraday cup used

Measurement #	$[I_H]$=A	$[V_E]$=V	$[V_{\pm B}]$=V		F.Cup
1	25	-7			2
2	25.5	-8			2
3	25.7	-8			2
4	25.8	-8	2345	-2230	1
5	26	-7			2
6	26.2	-6			2
7	26.5	-6	2280	-2290	1
8	26.7	-7			2
9	26	-2			2
10	26	-12			2

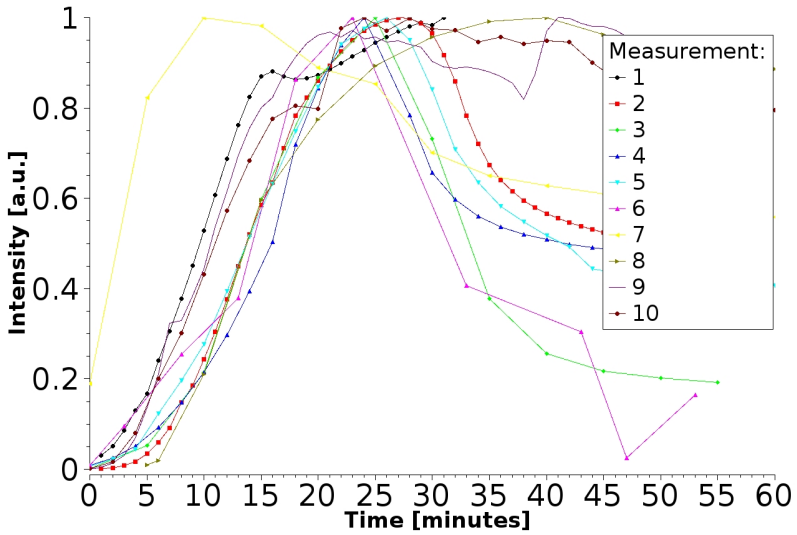

Figure 6.1: Normalized ion current stability measurements. Measurements 9 and 10 were made in the final set-up.

for the measurements are described in section 6.1. All stabilization curves are normalized to 1 because these measurements can not be used to compare the achievable maximum currents for each configuration for reasons described before. Measurements 5, 6 and 8 deviated from the other measurements in a way that the ion counting began before the HV had reached the maximum of 30 kV. This might have caused some error to the ion current during the first 10 minutes of the stabilization period, but it won't have any real effect on the important parts of

the stabilization curves as all the curves peak at times between 15 to 40 minutes. Measurement 7 was done with a malfunctioning Faraday cup 1 which caused a rise in the ion current of a factor of about two, but which should not interfere otherwise.

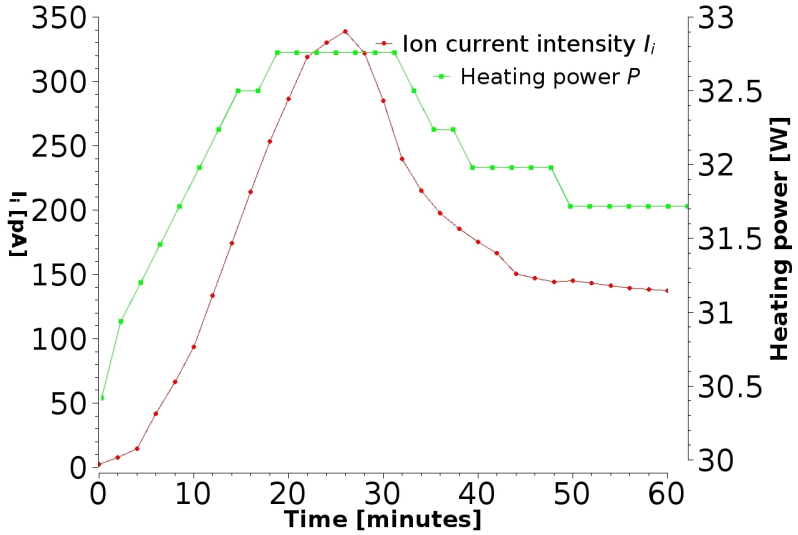

Figure 6.2: Example of the heating power -ion current relationship for I_H=26 A V_E=7 V

Measurement 1 was the first stability measurement and as fig 6.1 shows it differs significantly from the other measurements. The ion current does not have a peak after which it would start to decrease and eventually stabilize but it has a smaller peak followed by a small dip after which it begins to rise again. The reason for this might be, because the measurement was made in a quite early stage of the testing when the potassium supply was still almost full, that the large amount of Potassium available caused the peaking occur to much later in time. The measurement number 7 suffered from bad timing due to the fact that the measurement began after the HV had reached the 30 kV. This caused the curve for the measurement to peak much earlier than the other measurements because the ion current had started to rise well before the maximum HV had been reached.

If the measurement 1 is ignored the basic ion current stabilization curve is approximately the same shape for every configuration. The explanation for this behavior comes from the fact that the current ion source power system lacks a direct heating power control and regulation system. Figure 6.2 shows very good example how the heating power changes in time together with the ion current. Power stabilization curves for the configurations 4, 5, 6 and 8 are shown in figure 6.4. They all display the same behavior which is that the heating current peaks

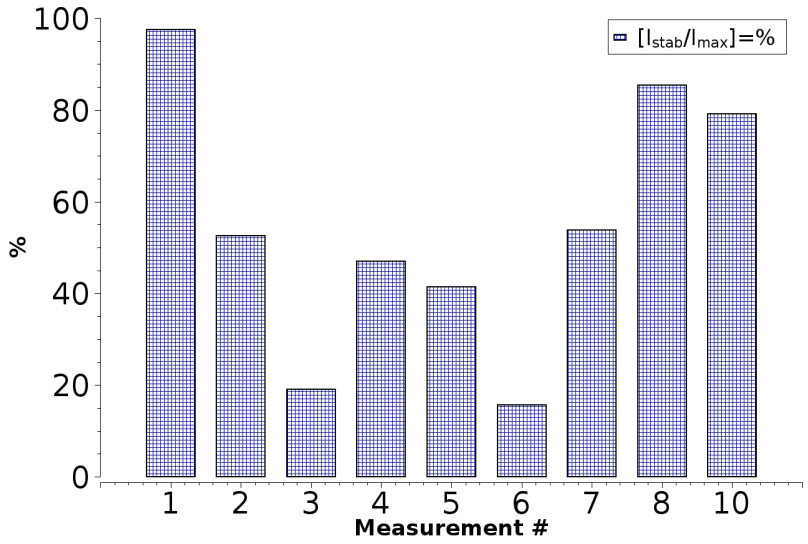

Figure 6.3: Comparsion of the peak ion current I_{max} and the stabilized ion current I_{stab} for test set-up measurements 1 to 8 and 10

at first and then decreases. A implementation of a power control system would probably remove this problem and decrease the gap between the peak current and the stabilized current that we see now (see Fig. 6.3).

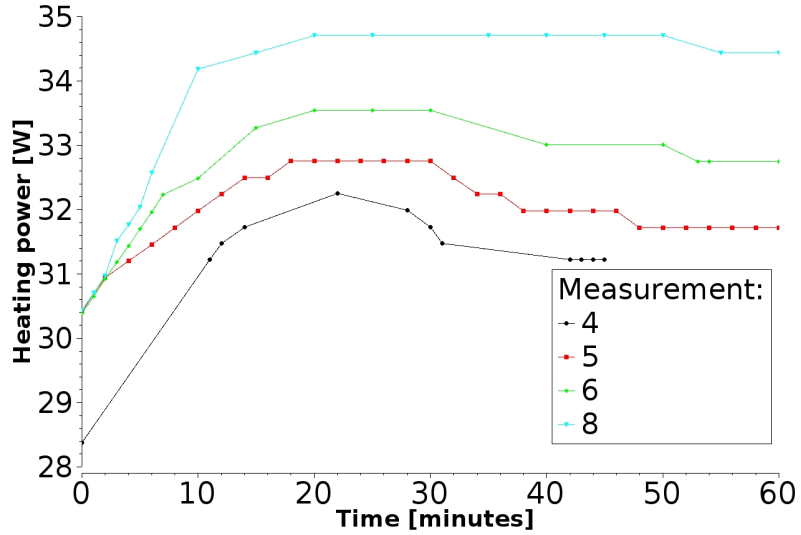

Figure 6.4: Heating power evolution during the stabilization period for measurements 4, 5, 6, 8.

During the measurement number 6 the current was unusually low and it's fluctu-

ations were up to 20 pA. This was the first measurement after the Faraday cup 1 was turned to y-direction, which might have had some effect on the current. The next measurement worked very well despite the malfunctioning Faraday cup 1. The ion current behavior in measurement 9 is also quite peculiar as the shape of the graph is more similar to the one in measurement 1 than the rest. The reason for this behavior might be in the fact that the V_E was -2 Volts, a value at which the beam shape is most asymmetrical (see Fig. 6.3). The ion current was also quite low on measurement number 8 but much higher than during measurement 6. The measurements 8 and 10 are quite similar in a way that the drop from the peak ion current to the stabilized ion current is quite low (see Fig. 6.3). This would probably also have been true for measurement 9 which was left out of this comparison due to high fluctuations in the ion current during the measurement. The reason for the low drop in the ion current might be that the ion source was already quite low in zeolite as it had by then been in use almost daily for about a month already. The measurements in figure 6.3 are in chronological order but the time gap or amount of operation between them is not uniform.

6.2 Ion current as a function of extraction voltage

Measurement configuration

The dependence of the ion current on the extraction voltage and bender voltages $I_i(V_E, V_{\pm B})$ was measured to find out the best value for the extraction voltage. The measurements were done from both Faraday cups 1 and 2 and from the HBL diagnostics unit Faraday cup (Diag.). For the measurements after the bender the effect of the bender voltages were also examined in both x- and y- directions. As in the beam current stabilization measurements, the absolute ion currents are irrelevant as the measurements spanned over a long time period.

The measurements were made after the beam had stabilized sufficiently so the changing current would not cause error. These measurements were also quite fast to perform so the the error caused by the slight fluctuation of the ion current was small. Measurements were done by first setting the extraction voltage V_E to -2 V which was the lowest value to which the extraction voltage source and the optical controller (see Fig. 5.8 items 3 and 5) allowed it to be set. The corresponding ion current was then read from the electrometer and the extraction voltage was increased to the next value. The increment step for the extraction voltage was from 1 to 2 volts when V_E was between -2 Volts and -20 Volts, after which the step size was increased as the ion current change became slower. The measurements were made up to V_E=-200 V. When the measurements were done after the bender,

Table 6.2: $I_i(V_E, V_{\pm B})$ -Measurement configurations

Measurement	$[I_H]$=V	$[V_{\pm B}]$=V		F.Cup
1	25			2
2	25.5			2
3a	25.8			2
3b		2345	-2320	1
4a				2
4b		2325	-2250	
4c		2120	-2420	
4d	26	2470	-2120	
4e		2280	-2290	1
4f		3205	-1510	
4g		1600	-2875	
5a		2280	-2290	1
5b	26.5	1880	-2600	
5c		2950	-1680	
6	26	2280	-2280	Diag.

the bender voltages were selected by first selecting some arbitrary extraction voltage and then finding suitable bender voltages so that the ion current was maximized.

In the test set-up the Faraday cup 1 linear feedthrough was set to 80 mm and in the final set up the HBL diagnostics Faraday cup was set to the center of the beamline. Also as in the previous section, the measurement with I_H=26.5 A suffered from the malfunctioning of Faraday cup 1, but as this affects only the measured ion current it is not relevant. The measurement configurations are displayed in table 6.2. Measurement 6 was performed after the ion source had bee installed in the HBL of the WITCH set-up.

Results

A total of 6 measurements were performed (see table 6.2). While the basic behaviour of the ion current is the same whether the measurement is done before the bender (see Fig. 6.5(a)) or after (see Fig. 6.5(b)), the peak is somewhat broader after the bender, while further the value of the extraction voltage at which the maximum ion current is achieved is lower when measured after the bender. The difference is quite significant as the shift can be up to 4 Volts (see Fig. 6.7). Also the value of the extraction voltage at, which the maximal ion current is achieved, varies between -6 and -4 Volts. The voltage source was not very accurate nor stable at these low voltages because it was designed to work at higher

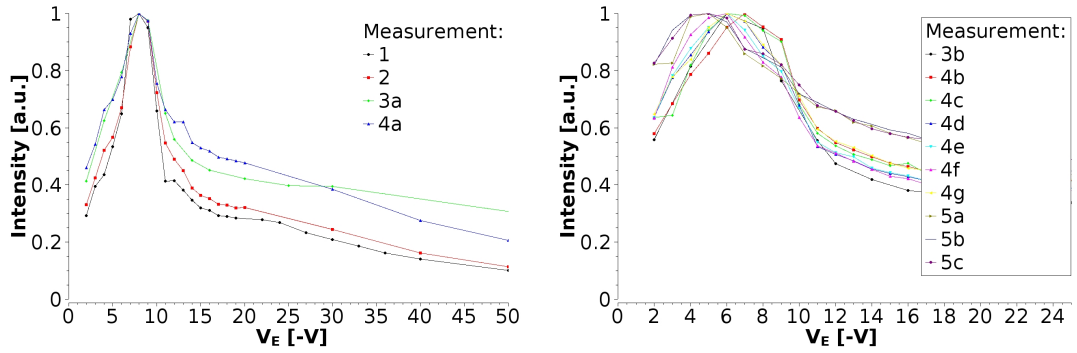

(a) (b)

Figure 6.5: Normalized results of $I_i(V_E)$ measured before the bender (a) and after the bender (b). Measurements were performed with the test set-up.

voltages. This introduces an error of about 1 Volt to the measurements in the range of extraction voltage [-2 V,-20 V]. Results for the whole V_E scale are shown in Fig. B.1. The ion current behaviour after V_E ∼-50V is uninteresting. The high ion currents in the measurements 5a, 5b and 5c can be partly explained by the malfunctioning Faraday cup. None of these measurements show any correlation between ion current maximum and bender voltages.

When the measurements were made with the Diag. Faraday cup the $I_i(V_E)$ graph (fig 6.6) shows a second peak in addition to the one around V_E=-7 V. The new peak is around V_E=-50 V and it is about 30 V wide and it was only observed with this Faraday cup. This indicates that the V_E affects the beam focusing in some way because the Faraday cup 1 is closer to the ion source bender than the Diag. Faraday cup.

6.3 Beam shape

Measurement configuration

The purpose of the beam shape measurements was to find out how different parameters of the ion source affect the shape and intensity of the beam. The measurements were done either by moving the Faraday cup 1 across the beam by of millimeter steps and logging the corresponding beam intensity or by moving a collimator across the Diag. Faraday cup. In order to be able to do the measurements in the y- direction in the test set-up, the diagnostics chamber had to be rotated 90 degrees. The measurements with the collimators were done after the

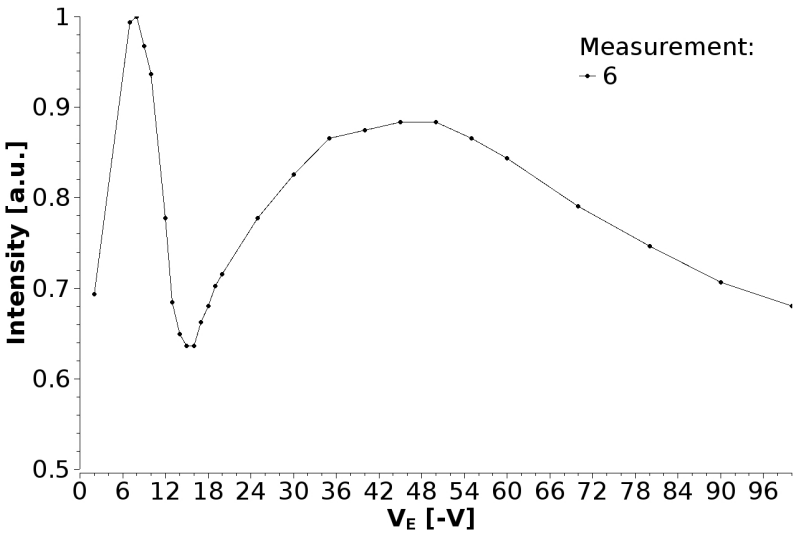

Figure 6.6: Normalized results of $I_i(V_E)$ measured with the Diag. Faraday cup

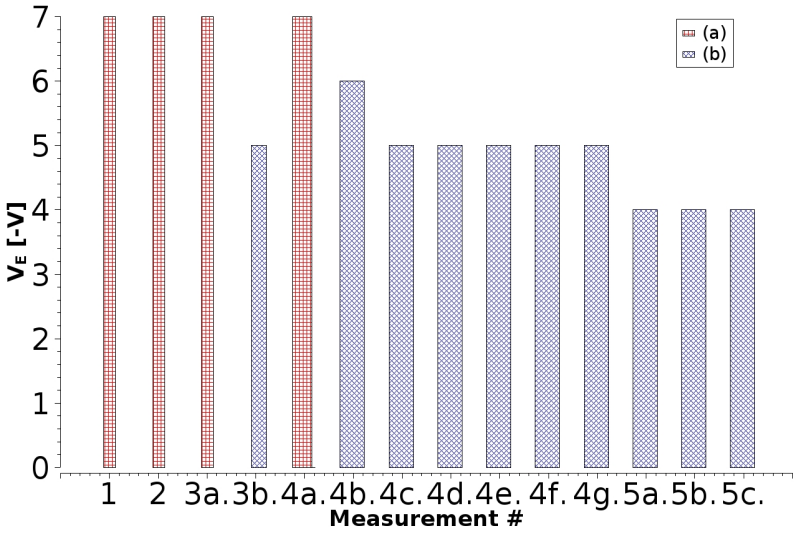

Figure 6.7: Extraction voltages for maximum ion current intensity in the test set-up. (a) Represents measurement performed before the ion source bender and (b) represents measurements made after the bender

Table 6.3: Beam width measurement configurations for the test set-up.

Measurement	$[I_H]$=A	$[V_{\pm B}]$=V		$[V_E]$=V
1	25.5	-2,410 -2,280 -1,830 -2,230	2,090 2,260 2,560 2,250	-7
2	25.7	-2,345	2,230	-2 -8 -12 -16
3	25.8	-2,340	2,230	-6 to -15 -17 -20
4	26	-2,120 -2,280 -3,205	2,420 2,290 1,510	-10 to -16 25
5	26.5	-1,180 -2,280 -3,950	2,600 2,290 1,680	-2 to -16 20

ion source had been installed in to the HBL. The measurements consisted of measuring the beam shape for different bender voltages and extraction voltages. The bender voltages were chosen by first applying some arbitary voltage to the other bender plate and then tuning the voltage on the other plate until a peak in the ion current was found. The Faraday cup 1 was also in a arbitary position during this, but of course in such a way that the beam could reach it. The parameters for the measurements with the Faraday cup 1 in the test set-up are displayed in table 6.3. The table indicates the bender voltage values $V_{\pm B}$ for which the beam shape was measured with the corresponding extraction voltage V_E scale.

The measurements with the Diag. Faraday cup were made by moving the cup to the center of the beamline and then moving the wanted collimator hole across the Faraday cup 1 mm a time and measuring the corresponding ion current. All the beam shape measurements were done in vertical direction with $[V_{+B}]$=2280 V $[V_{-B}]$=-2280 V and I_H=26 A. The beam shape was measured with collimator holes 20 mm, 8 mm, 5 mm and the slit for V_E= -12 V, and with 20 mm and 8 mm collimator holes for V_E= -45 V.

The beam was also directed through the 90° bender in to the VBL and measured with the segmented anode MCP detector on the VBL diagnostics unit. In order to do this the kicker and bender electrodes on the HBL were powered and the bender

electrodes on the ion source were pulsed with a Behlke controller. The pulsing was done because the MCP cannot handle well a continuous beam. The pulsing worked so that for every second during a 997 ms period the ions were rejected and for 3 ms the were allowed to pass on to the MCP. The beam intensity was measured from the each anode segment separatelly. The MCP anode voltage was set to 1.75 kV and the beam was measured for V_E= -7 V, -12 V and -45 V

Results

Measurements with a Faraday cup give a graph from which the actual beam width can be extracted using the equations 4.21 and 4.22. For example in figure 6.9(b) a measurement is shown that was done with V_E= -11 V. By approximating the width of the flat part y=8 mm±1 mm and using equation 4.21 where D=16.5 mm±0.1 mm, the actual width of the beam becomes

$$R = 16.5mm - 8mm = 8.5mm. \tag{6.1}$$

The error for the beam width can be calculated using the equation 4.24 by

$$\delta R = \sqrt{1^2 + 0.1^2}mm, \tag{6.2}$$

which gives the beam width with error $R = 8.5mm \pm 1mm$. It's easy to see that as the flat part of the graph gets smaller the beam gets wider. For example figure 6.13(a) shows that the beam width is about the same as the diameter of the Faraday cup when using the V_E=7 V, which provides the highest current at the bottom Faraday cup (see sec. 6.2). It also shows that the bender voltages have no impact on the beam shape in x-direction. The beam widths as a function of extraction voltage with V_{-B}=-2280 V and V_{+B}=2290 V in x- and y-direction are presented in figure 6.10. From this figure it can be seen that the beam shape is a symmetrical sphere with radius of about 8.5 mm when V_E=-10.7 V. The value is only a crude estimate of the actual beam shap and size as the center point for the beam is approximately at 79.5 mm±1 mm in x-direction and at 85 mm±1 mm in y-direction. This means that the beam is not on the center of the beamline, which in turn means that the beam shape calculations probably contain a larger error than the adopted 1 mm, at least when measuring in the y-direction.

By comparing the figures 6.8(a) and 6.8(c) with 6.8(b) and figures 6.9(a) and 6.9(c) with 6.9(b) it's obvious that that bender voltages have no visible effect on the beam width and there's no need to study the actual beam width separately on these cases. They also look quite similar with the simulated result of the beam width shown in figure 4.6(a). Measurement number 5 was done in y-direction and the results differ from the measurements done in x-direction. It seems that the

beam shape stays quite good for the whole scale of extraction voltages, but it also shows that if the bender voltages are not symmetrical the beam intensities begin to separate themselves into three distinctive bunches (see Fig.'s 6.9(a) and 6.9(c)) depending on the extraction voltage. The first bunch corresponds to the extraction voltages that provide the maximum current when measured after the bender. The second bunch includes those extraction voltages that are on the steeps slopes at both sides of the I(V_E)- graph (see Fig. 6.5(b)) and the rest are on the gentle slope. The measurements in y-direction also indicate that beam is shifted downwards in the y-direction if the bender voltages are asymmetrical. The figures 6.9(a) and 6.9(c) and 6.9(b) show that the shift can be as big as about 4 mm, and the direction of the shift is the same in both cases with asymmetrical bender voltages. There is no such effect in the x-direction.

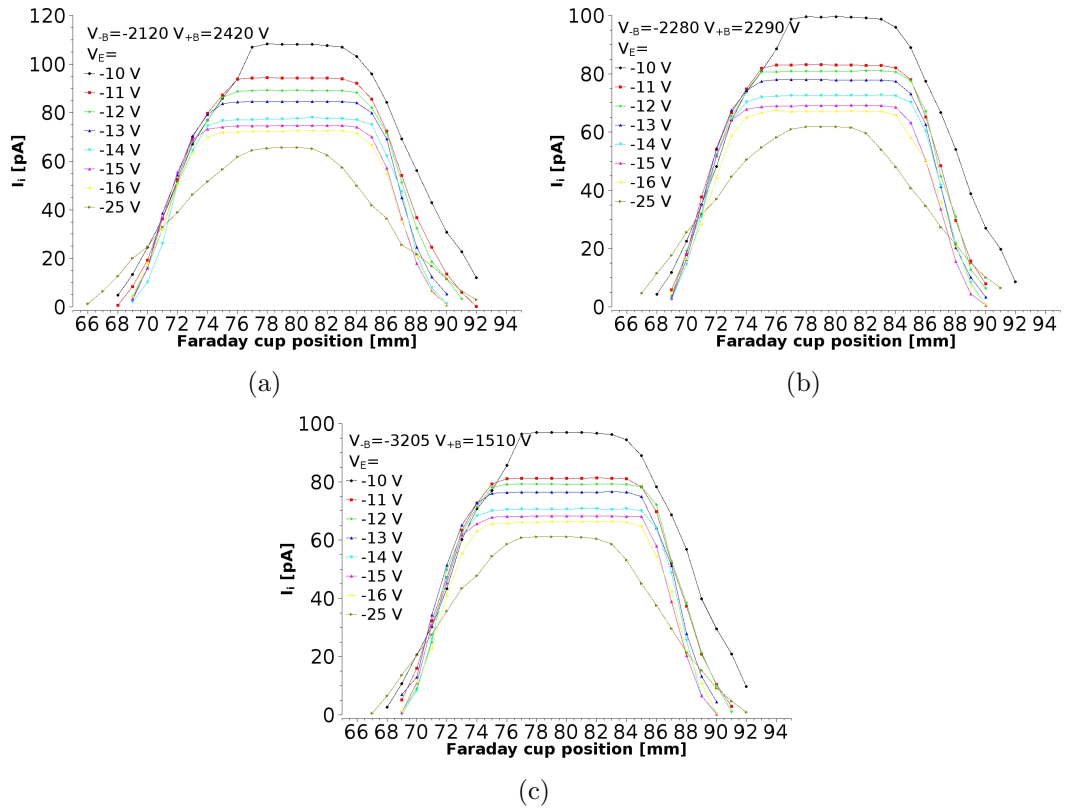

Figure 6.8: Beam shape in x-direction with $|V_{-B}| < V_{+B}|$ (a), $|V_{-B}| \sim V_{+B}|$ (b) and $|V_{-B}| > V_{+B}|$. Measurement #4 in table 6.3.

The beam shape measurements 1 to 5 discussed so far were all performed with the test set-up. In what follows, the beam shape measurements that were performed in the HBL and the VBL after the ion source had been installed in to the WITCH

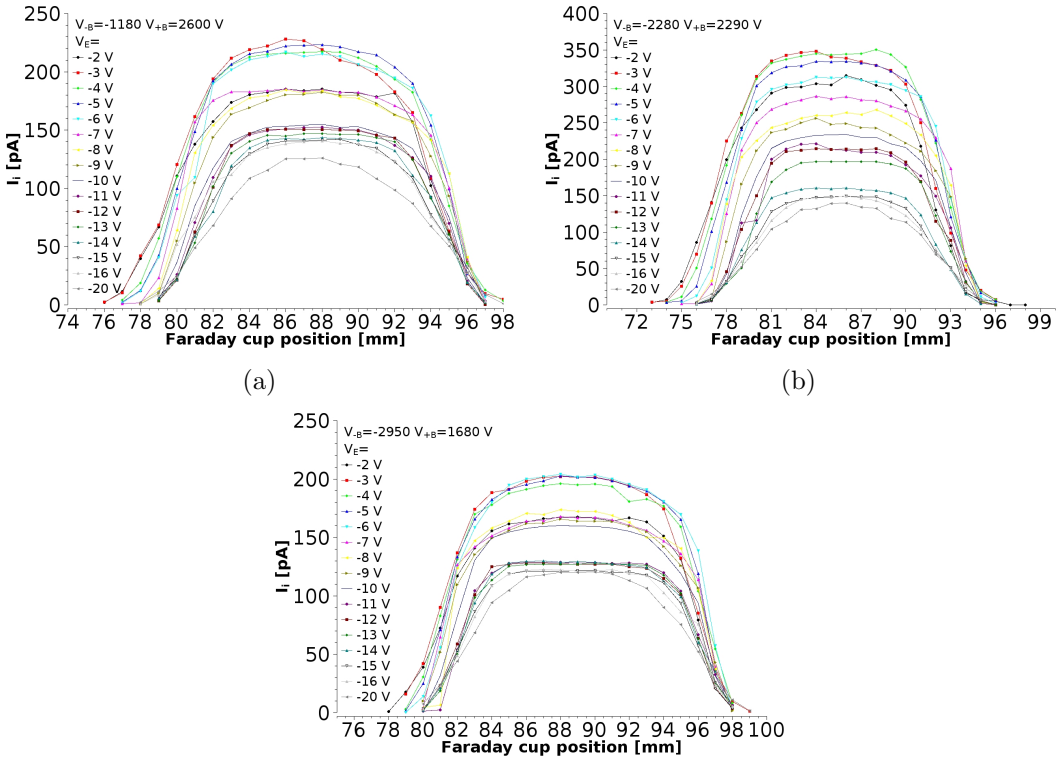

Figure 6.9: Beam shape in y-direction with $|V_{-B}| < V_{+B}|$ (a) , $|V_{-B}| \sim V_{+B}|$ (b) and $|V_{-B}| > V_{+B}|$. Measurement #5 in table 6.3.

set-up, will be discussed.

Figure 6.11 shows the beam profile measured with different collimator holes for two different V_E's. The only collimator hole to give some reasonable results is the 20 mm hole for which the graph is positioned quite symmetrically around the center point of the hole. Other measurements are less symmetrical and the slit measurement is totally incomprehensible. The assymetric graphs for V_E=-12 V, 5 mm hole and V_E=-45 V, 8 mm hole indicate that the beam is shifted from the beamline center in x-direction, while the extraction voltage V_E=-45 V seems also to distort the beam shape. The V_E= -12 V measurement for 8 mm hole indicates that the beam diameter would be quite close to the diameter of the hole. By calculating the beam width with equations 4.21 and 4.24 for measurement V_E= -12 V, 20 mm we indeed get R=10.6 mm±1 mm

Finally the figures 6.12(a) and 6.12(b) show the beam intensity on each wire of the segmented anode MCP detector on the VBL diagnostics unit. The beam is clearly not centered in the direction of the A-row. It is expected that this deviation can

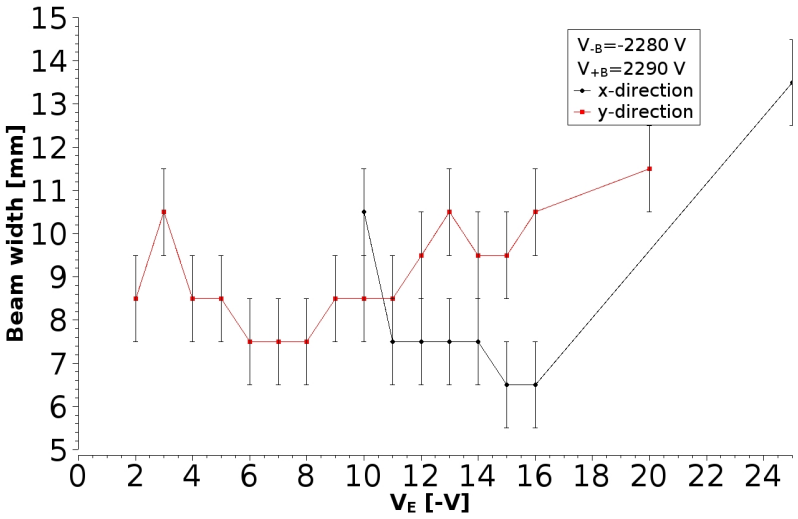

Figure 6.10: Beam width in x- and y -directions

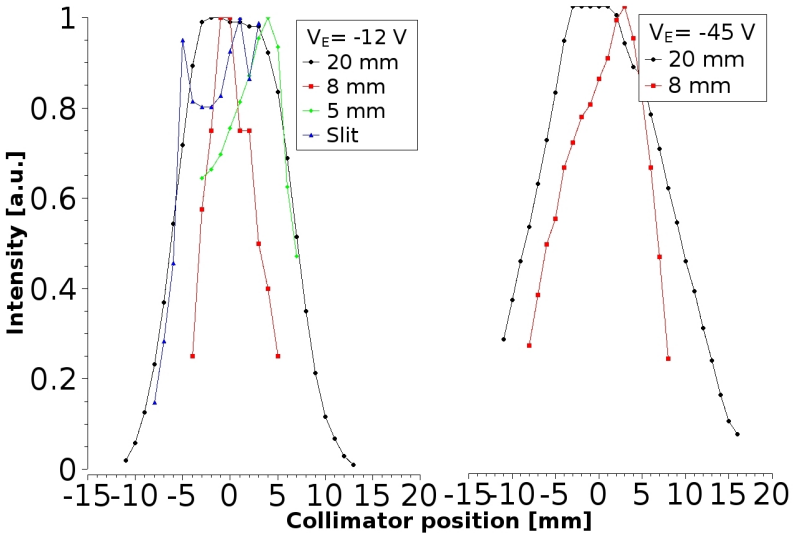

Figure 6.11: Beam width measurement for collimator diameters of 20 mm, 8 mm, 5 mm and for a slit collimator for V_E=-12 V and -45 V. Collimator position relative to the beamline center

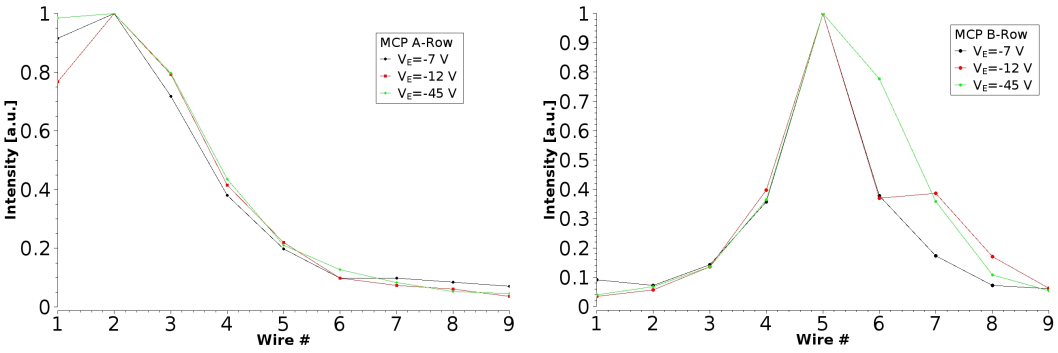

(a) (b)

Figure 6.12: Beam intensity distribution on the A-row (a) and on the B-row (b) of the segmented anode MCP detector in the VBL diagnostics unit.

be corrected using the available steering electrodes in the HBL and VBL.

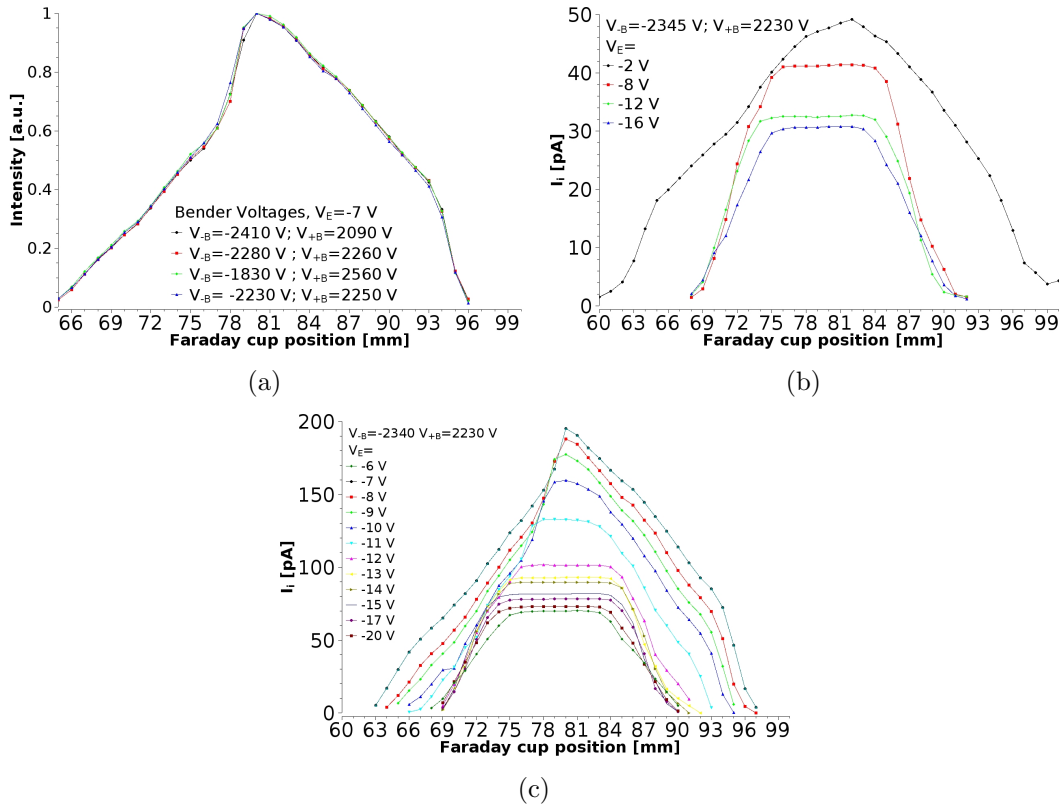

Figure 6.13: The beam shape as a function of bender voltages (a) and as a function of the extraction voltage (b and c). A, b and c correspond to measurements 1, 2 and 3 in table 6.3 respectively.

Chapter 7

Discussion

The purpose of this work was to study the properties of the WITCH off-line tuning ion source and to find optimal operation parameters for the extraction voltage and for the bender voltages. The tests began on a test set-up and continued after the ion source had been incorporated into the HBL. This provided two slightly different environments for the tests.

The tests showed that the most relevant parameter affecting the beam shape is the extraction voltage and that it affects the beam shape differently depending on the direction. The best value was found to be V_E=-10.7 V which provides a beam with a spherical crosscut with a diameter of 8.5 mm± 1 mm but with a ion current that is about one third of the maximum ion current which is achieved with $V_E \in$[-5, -7] V (see Fig. 6.5(b)). The size mentioned is this at the Faraday cup 1, but already at the Diag. Faraday cup, which is on slightly further in the beamline, the beam size in y-direction is about 10.6 mm±1 mm at V_E= -12 V. The beam width would be 7.5 mm±1 mm at V_E= -12 V when measured with the Faraday cup 1.

The beam is not centered on the beamline central axis as can be seen from figures 6.8(b) and 6.9(b). The beam center point seems to be approximately at 79.5 mm±1 mm in x-direction and at 85 mm±1 mm in y-direction when measured with the Faraday cup 1. This means that the the beam is quite well centered in y- direction when symmetrical beder voltages as the beamline central axis is approximately at 84 mm in both x- and y-directions. This shift in the x-direction is also apparent on the A-row MCP measurement in figure 6.12(a). This means that the beam must be shifted using the steerer electrodes on the beamlines and that the beam width measurements are erroneous as the beam is not scanned along it's axis.

The extraction voltage affects the focusing of the beam after the ion source bender. This can be seen for example from figure 6.6 at which a new ion current

maximum has appeared around V_E=50 V when measuring with the Diag. Faraday cup. The beam shape in the new maximum is a lot worse than in the previous maximum as can be seen in figure 6.11. The beam cross section area should be as small as possible and our measurements give some directions for choosing the proper extraction voltages for finding it. In the end the final value is determined by the overall effect of the different electrodes in the HBL and in the VBL. The ion source bender voltages seem not to have any significant effect on the beam shape but they shift the beam downwards if they are asymmetrical.

The lack of the power regulation caused very obvious problems during the tests. It took a very long time for ion the current to become sufficiently stabilized in order to perform measurements, while even then the current continued to fluctuate (see Fig. 6.2). The lack of power regulation also reduced the achievable ion current up to 80 % when compared with the peak current. As the beam intensity difference between Faraday cup 2 and the Diag. Faraday cup is about 36 % and the transfer efficiency through the 90° bender is about 66 %, there's a real need to improve the original ion current. If the ion source produces a stabile ion current of 150 pA the effective ion current is merely 4,5 pA because the beam has to be pulsed. This corresponds to about $3{\cdot}10^6$ ions. The transfer effeciency from the ion source to the VBL is about 66% and the transfer effeciency onwards to the MCP is about $2{,}5{\cdot}10^{-2}$% [62] which means that less than 1000 ions will be detected. For example, if the power regulation is implemented and it will work as expected, the ion source should provide ion currents of at least 350 pA. This current was seen as a one peak value during the ion current stabilization measurements. Highest ion currents observed reached about 700 pA during the first test runs of the ion source. This means that only by refilling the potassium zeolithe and implementing the power regulation, an increase of almost a factor of 5 might be achivable. The alingment of the ion source will naturally improve the overall transfer efficiency thus increasing the number of the ions detected. 10 000 ions detected at the MCP would be a very good and usefull for the tuning of the WITCH set-up.

The future work on the ion source should consist in the improvement of the achievable ion current in which the power regulation will play a major role. Also the cause for the beam displacement from the beamline central axis must be addressed. The reason for the displacement might be that the ion source is slightly tilted or that there's some fundamental error in the design. The last option is less probable as the ion source is an almost exact copy of the REX-TRAP ion source. Of cource the beam can be moved to the beamline central axis by using the electrodes in the beamline but this then reduces the value of the ion source as these settings cannot be applied to the actual radioactive beam. Thus, the alignment of the ion source has to be carfully checked. If possible it would be good to install a set of x- and y-deflection plates in front of the ion source bender

in order to correct for the shift in the x-direction. All and all the ion source works quite well and by eliminating these problems it will be a great tool for the WITCH set-up tuning.

Appendix A

Bender power source data

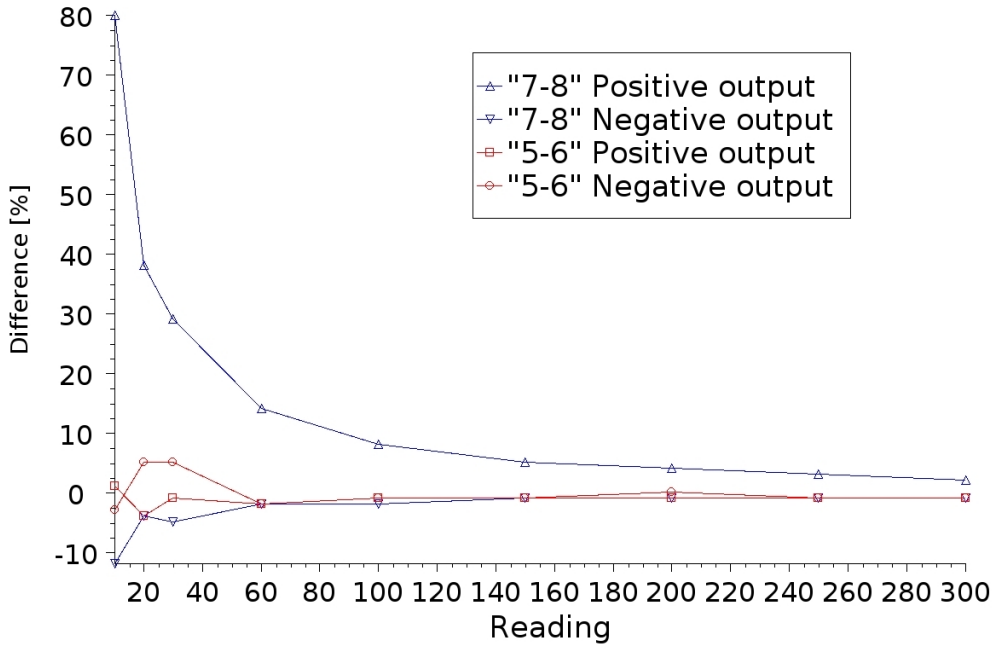

Figure A.1: Difference between the IKS bender power source reading and the actual voltage for power sources marked '5-6' and '7-8'(see figure 5.8 item 7).

Appendix B

Additional results

B.1 $I_I(V_E)$

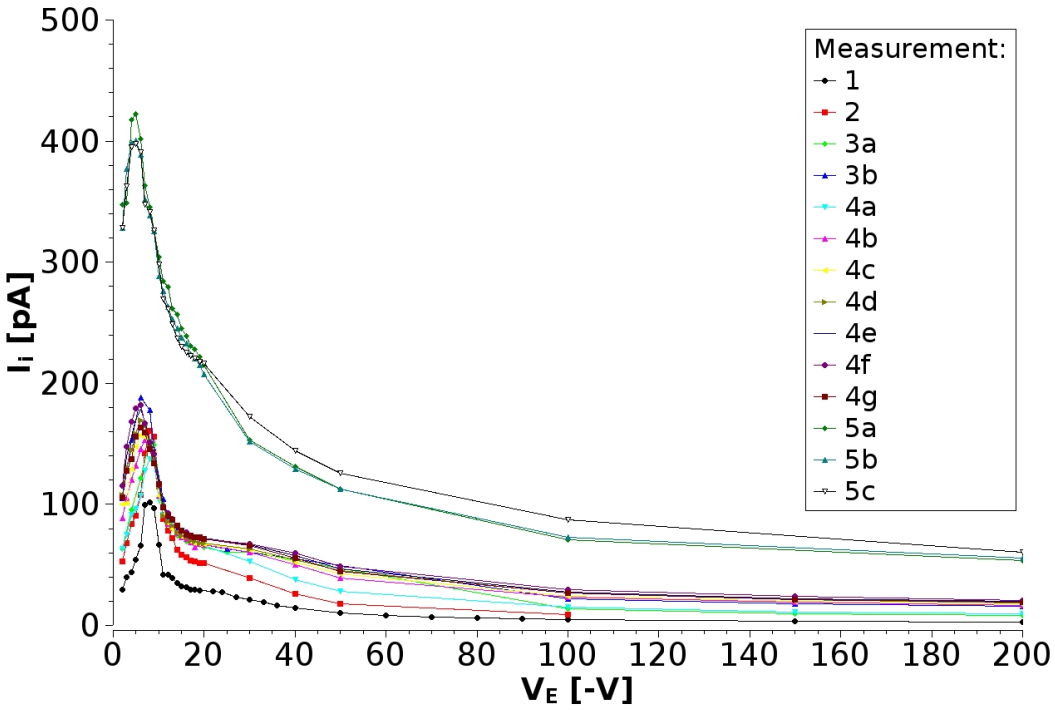

Figure B.1: Ion currents as a function of extraction voltage, $V_E \in$[2,200]V.

Appendix C

Photos of the WITCH Ion Source and the WITCH set-up

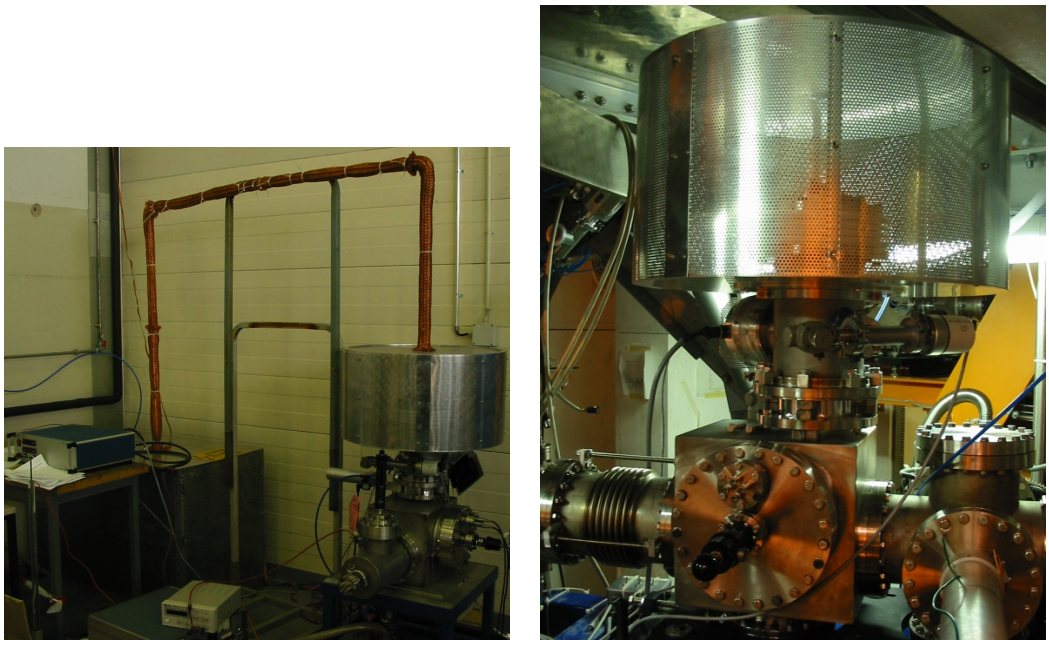

(a) (b)

Figure C.1: The WITCH offline tuning ion source test (a) and final (b) set-up

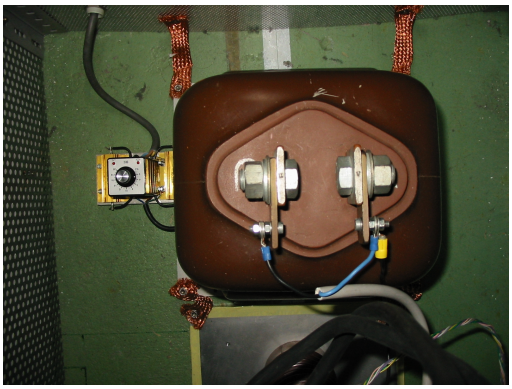

(a)

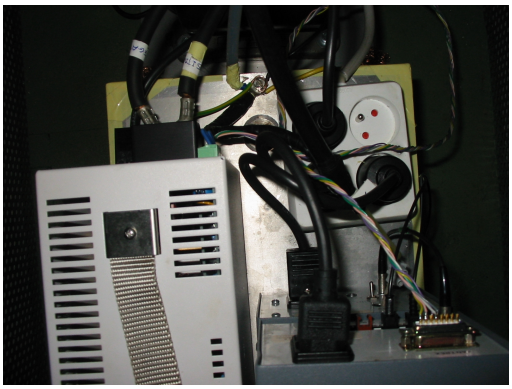

(b)

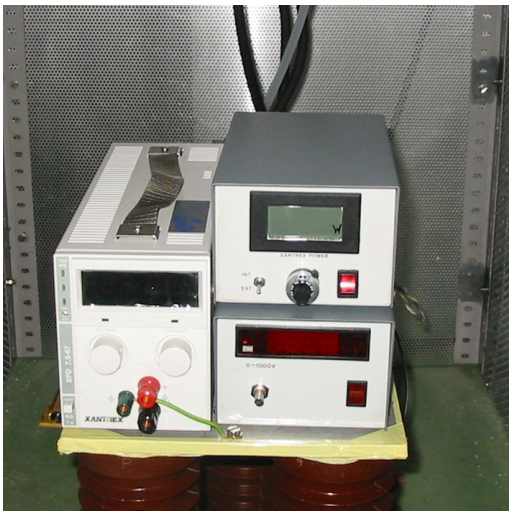

(c)

Figure C.2: The WITCH ion source electronics: Mosef-Glasev transformer (a), high voltage platform (b) and heating and extraction power sources and controllers (c).

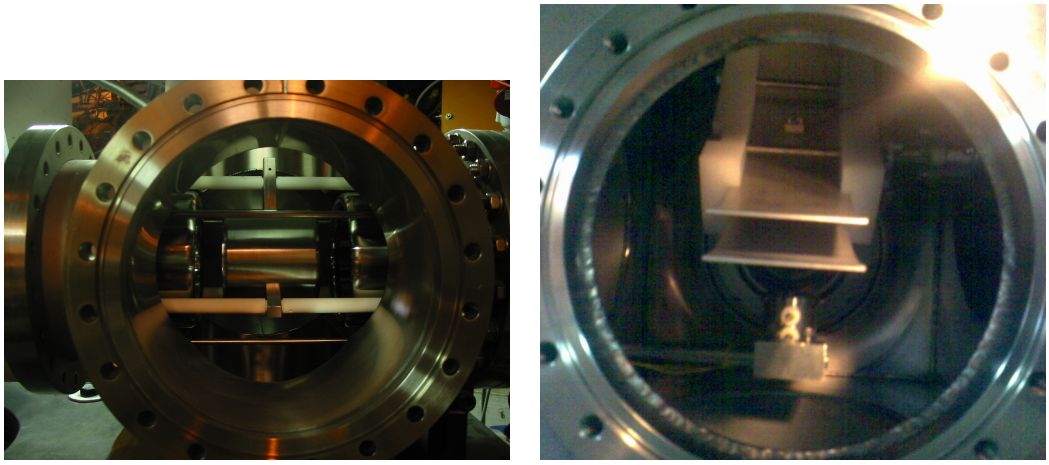

(a) (b)

Figure C.3: The WITCH Einzel lens (a) and the bender and the Faraday cup 2 of the WITCH Ion source (b).

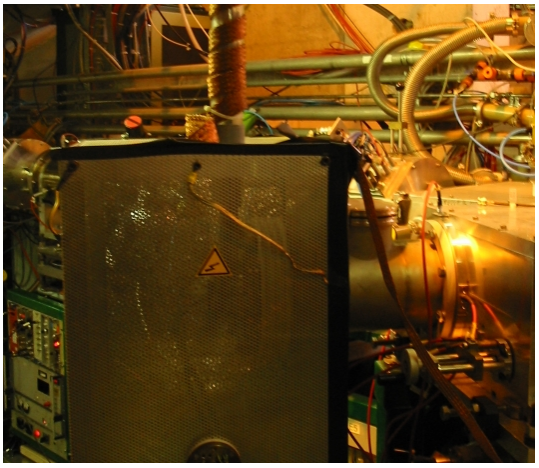

Figure C.4: The REX-TRAP ion source

Bibliography

[1] H. Winter et al. Simple demonstration of storing macroscopic particles in a "paul trap". *Am. J. Phys.*, 59, 1991.

[2] Bavo Delauré. *Development of a Penning Trap based Set-up for Precision Tests of the Standard Model*. PhD thesis, Leuven Katholieke Universiteit, 2004.

[3] Valentine L. Telegdi. Present experimental evidence for a fermi interaction in muon capture. *Phys. Rev. Lett.*, 8(8):327–328, Apr 1962.

[4] T. D. Lee and C. N. Yang. Question of parity conservation in weak interactions. *Phys. Rev.*, 104(1):254–258, Oct 1956.

[5] X Fléchard et al. The LPCTrap facility: A transparent paul trap for the search of exotic couplings in the beta decay of radioactive $^6He^+$ ions. volume 58, pages 431–434. 13th International Conference on the Physics of Highly Charged Ions, 2007.

[6] E.Ya. Zanberg and N.I. Ionov. *Surface Ionization*. Israel Program for Scientific Tanslations, 1971.

[7] ISOLDE, 2006. `http://isolde.web.cern.ch/ISOLDE/`.

[8] Erich Kugler. The ISOLDE facility. *Hyperfine Interactions*, 129:23–42, 2000.

[9] Valentin Kozlov. *WITCH, a Penning trap for weak interaction studies*. PhD thesis, Leuven Katholieke Universiteit, 2005.

[10] CERN accelerators. `http://ps-div.web.cern.ch/ps-div/PSComplex/accelerators.pdf`.

[11] J. D. Jackson, S. B. Treiman, and Jr. H. W. Wyld. Possible tests of time reversal invariance in beta decay. *Phys. Rev.*, 106:517–521, 1957.

[12] M. Beck et al. WITCH: a recoil spectrometer for weak interaction and nuclear physics studies. *Nucl. Inst. and Meth. A*, 503:567–579, 2003.

[13] J. S. Allen et al. Determination of beta-decay interaction from electron-neutrino angular colleration measurements. *Phys. Rev.*, 116(1):134–143, 1959.

[14] C. H. Johnson, Frances Pleasonton, and T. A. Carlson. Precision measurement of the recoil energy spectrum from the decay of He^3. *Phys. Rev.*, 132(3):1149–1163, 1963.

[15] A. García et al. Positron-neutrino correlations in ^{32}Ar and ^{33}Ar decays: Probes of scalar weak currents and nuclear isospin mixing. *Hyperfine Interactions*, 129:237–248, 2000.
[16] E. G. Adelberger et al. Positron-neutrino correlation in the $0^+ \rightarrow 0^+$ decay of ^{32}Ar. *Phys. Rev. Lett.*, 83:1299–1302, 1999.
[17] N. Severijns. Weak interaction studies by precision experiments in nuclear beta decay. 2001.
[18] V.Yu. Kozlov et al. The WITCH experiment: Completion of a set-up to investigate the structure of weak interactions with a penning trap. *International Journal of Mass Spectrometry*, 251:159–172, 2006.
[19] V.Yu. Kozlov et al. Physics and present status of the WITCH experiment. *Physics of Atomic Nuclei*, 6:1112–1118, 2004.
[20] M. Herrero. The standard model. Presented on 10th NATO ASI on Techniques and Concepts of High-Energy Physics, Jun 1998.
[21] Makoto Kobayashi and Toshihide Maskawa. CP violation in the renormalizable theory of weak interaction. *Prog. Theor. Phys.*, 49:652–657, 1973.
[22] Elementary particles. `http://en.wikipedia.org/wiki/Elementary_particles`.
[23] E. Noether. Invariant variation problems. *Transport Theory and Statistical Physics*, 1(3):183–207, 1971. M. A. Tavel's English translation of "Invariante Variationsprobleme" Nachr. d. König. Gesellsch d. Wiss. zu Göttingen, Math-phys. Klasse, 235-257 (1918).
[24] K. Eskola. Particle physics 1, 2006. Lecture notes.
[25] D.E. Groom et al. 11. The Cabibbo-Kobayashi-Maskawa quark-mixing matrix. *The European Physical Journal*, C15:1+, 2000. `http://pdg.lbl.gov`.
[26] D.E. Groom et al. 10. Electroweak model and constraints on new physics. *The European Physical Journal*, C15:1+, 2000. `http://pdg.lbl.gov`.
[27] Y. Ashie et al. Evidence for an oscillatory signature in atmospheric neutrino oscillations. *Phys. Rev. Lett.*, 93(10):101801–1, 2004.
[28] Rahul Sinha, Basudha Misra, and Wei-Shu Hou. Has new physics already been seen in B_d meson decays? *Phys. Rev. Lett.*, 97:131802–1, 2006.
[29] N. Severijns and M. Beck. Tests of the standard electroweak model in beta decay. *Rev. Mod. Phys.*, 78:991–1040, 2006.
[30] N. Severijns et al. Fundamental weak interaction studies using polarised nuclei and ion traps. *Hyperfine Interactions*, 129:223–236, 2000.
[31] P. Dessagne. Nuclear decay studies and weak interactions. *Nucl. Phys. A*, 701, 2002.
[32] Kenneth S. Krane. *Introductory Nuclear Physics*. John Wiley and Sons, 1988.
[33] F. Ames et al. Cooling of radioactive ions with the Penning trap REXTRAP. *Nucl. Inst. and Meth. A*, 538:17–32, 2005.

[34] D. Habs et al. The REX-ISOLDE project. *Hyperfine Interactions*, 129:43–66, 2000.

[35] O. Forstner. *Beam-Preparation with REXTRAP for the REX-ISOLDE Experiment*. PhD thesis, 2001. Presented on 10 Sep 2001.

[36] Einzel lens. `http://en.wikipedia.org/wiki/Einzel_lens`.

[37] F. Herfurth et al. A linear radiofrequency ion trap for accumulation, bunching, and emittance improvement of radioactive ion beams. *Nucl. Inst. and Meth. A*, 469:254–275, 2001.

[38] The Faraday. `http://www.casetechnology.com/implanter/faraday.html`.

[39] Joseph Ladislas Wiza. Microchannel plate detectors. *Nucl. Instr. and Meth.*, 162:587–601, 1979.

[40] Valentin Kozlov, 2007. Private Communication.

[41] Reijo Saintola. Electromagnetic particle traps. Thesis for the degree of licentiate of philosophy, University of Jyväskylä, 1993.

[42] Klaus Blaum. A high-accuracy mass spectrometry with stored ions. *Physics Reports*, 425(1):1–78, 2006.

[43] Wolfgang Paul. Electromagnetic traps for charged and neutral particles. *Rev. Mod. Phys.*, 62(3):531–540, Jul 1990.

[44] The WITCH experiment website. `http://fys.kuleuven.be/iks/ko/research/witch/index.phtml`.

[45] S. Coeck et al. Microchannel plate response to high-intensity ion bunches. *Nucl. Inst. and Meth. A*, 557:516–522, 2005.

[46] L. Stenberg. Pintaionisaatioon perustuvat ionilähteet. Master's thesis, University of Jyväskylä, 1978.

[47] U. Köster. Progress in ion source development for on-line separators. *Nucl. Phys. A*, 701:441c–451c, 2002.

[48] J. Merikoski. Material physics 1, 2004. Lecture notes.

[49] C.Kittel. *Introduction to solid state physics, 5th edition*. John Wiley and Sons, 1976.

[50] R. Kirchner. Progress in ion source development for on-line separators. *Nucl. Inst. and Meth. A*, 186(1-2), 1981.

[51] J.B.Tatum. `http://astrowww.phys.uvic.ca/~tatum/phys317/notes/thermod16.pdf`.

[52] J. Lettry et al. Recent developments of the ISOLDE laser ion source. *Review of Scientific Instruments*, 69:761–763, 1998.

[53] U. Köster, O. Kester, and D. Habs. Ion sources for fission fragment accelerators. *Rev. Sci. Instrum. A*, 69:737, 1998.

[54] N. Angert. Ion sources. CAS - CERN Accelerator School : 5th General accelerator physics course, Sep 1992.

[55] T. Ropponen. ECR-ionilähteiden plasmapotentiaali ja ambipolaarinen diffuusio. Master's thesis, University of Jyväskylä, 2005.
[56] J. Taylor. *An Introduction to Error Analysis: The Study of Uncertainties in Physical Measurements*. University Science Books, 1982.
[57] Circular segment. `http://mathworld.wolfram.com/CircularSegment.html`.
[58] Circle-circle intersection. `http://mathworld.wolfram.com/Circle-CircleIntersection.html`.
[59] Pfeiffer Vacuum. Mass spectrometer catalogue, 2005. `www.pfeiffer-vacuum.com/filepool/2/File/MS_Catalog_E.pdf`.
[60] S. Eylon et al. K+ ion source for the heavy ion induction linac system experiment ILSE. Particle Accelerator Conference, 1993.
[61] M. Herbane, 2006. Private Communication.
[62] V.Yu. Kozlov et al. The witch experiment: towards weak interactions studies. status and prospects. `http://www.citebase.org/abstract?id=oai:arXiv.org:nucl-ex/0701007`, 2007.